Article submitted to: High Power Laser Science and Engineering, 2023 *May 18, 2023*

X-ray polarimetry and its application to strong-field QED

Qiqi Yu[1,2], Dirui Xu[3], Baifei Shen[1], Thomas E. Cowan[2,4], and Hans-Peter Schlenvoigt[2]

[1]*Shanghai Normal University, 200234 Shanghai, People's Republic of China*
[2]*Helmholtz-Zentrum Dresden – Rossendorf, 01328 Dresden, Germany*
[3]*State Key Laboratory of High Field Laser Physics, Shanghai Institute of Optics and Fine Mechanics, Chinese Academy of Sciences, 201800 Shanghai, China*
[4]*Technische Universität Dresden, 01062 Dresden, Germany*

Abstract
Polarimetry is a highly sensitive method to quantify changes of the polarization state of light when passing through matter and is therefore widely applied in material science. The progress of synchrotron and X-Ray Free Electron Laser (XFEL) sources has led to significant developments of X-ray polarizers, opening perspectives for new applications of polarimetry to study source and beamline parameters as well as sample characteristics. X-ray polarimetry has shown to date a polarization purity of $<1.4 \cdot 10^{-11}$, enabling detection of very small signals from ultrafast phenomena. A prominent application is the detection of vacuum birefringence. Vacuum birefringence is predicted in Quantum Electrodynamics (QED) and expected to be probed by combining an XFEL with a petawatt-class optical laser. We review how source and optical elements affect X-ray polarimeters in general and what qualities are required for detection of vacuum birefringence.

Keywords: X-rays, polarizer, polarimetry, birefringence, QED

1. Introduction

Polarization is one of the fundamental characteristics of electromagnetic radiation[1]. Polarimetry, the quantitative determination of the polarization state, is a multifunctional and sensitive method to study light-matter interaction. In general, a polarimeter consists of two polarizers – called polarizer and analyzer – and their linear polarization transmission directions have an angle to each other, usually using orthogonal polarization settings, refer to Figure 1: A beam from the light source becomes linearly polarized by the polarizer. The linearly polarized light undergoes a change in polarization as it passes through the anisotropic sample. Only the beam component whose polarization meets the transmission direction of the analyzer can finally pass through the analyzer and can be detected by the detector. The physical properties of the sample can be obtained by detecting the change in polarization of the beam before and after it passes through the sample.

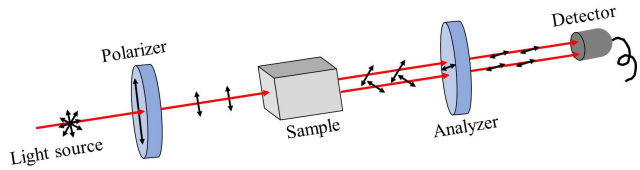

Figure 1: Basic scheme of polarimetry. Essential is the pair of polarizers with a different and variable orientation to each other to study the effect of a sample in between onto the polarization.

Polarimetry with high resolution, which breaks the limitations of low spatial resolution inherent in traditional measurement methods, is an emerging detection tool for atmospheric remote sensing, astronomy, biomedical diagnostics, and much more[2,3]. For instance, by combining with multispectral and multi-angle functionality, polarimetry allows for the analysis of aerosol's microphysical properties and chemical composition in atmospheric remote sensing[4,5]. In biomedical diagnostics, the degree of polarization depends on the properties of the biological tissues. Polarimetry is a diagnostic for tissue properties and provides a useful way for

Correspondence to: h.schlenvoigt@hzdr.de and bfshen@shnu.edu.cn

10.1017/hpl.2023.45

early cancer detection[6].

At the beginning of the 20th century, Barkla[7–9] pointed out that X-rays are polarized. X-ray polarimetry has been developed gradually in many research fields because of the short wavelength and great penetration of X-rays[10,11]. For the detection of magnetic fields, polarized X-rays have the appropriate ability to explore the features of magnetic structures in structural magnetism and the X-ray polarization can discriminate chiral from helimagnetic structures[12–15]. In the measurement of X-ray optical activity, Siddons *et al.*[16] successfully observed the optical activity and obtained $2\,\mathrm{mrad}$ rotations in a chiral organometallic compound.

Moreover, polarimetry with high sensitivity can be applied to explore the nonlinear properties of vacuum. In the QED description of vacuum[17], virtual particle-antiparticle pairs, called quantum fluctuations, are allowed for ultra-short times. In strong external electric or magnetic fields, these virtual particle pairs can be partially aligned, resulting in an optical property of vacuum.

In essence, fields **E** and **B** yield higher-order terms of the Lagrangian $\mathcal{L}$ describing the wave propagation[18–21] where the first order correction reads (in natural units $\hbar = c = 1$) as

$$\delta\mathcal{L} = \xi\left[(\mathbf{E}^2 - \mathbf{B}^2)^2 + 7(\mathbf{E}\cdot\mathbf{B})^2\right] , \tag{1}$$

where ξ is a normalization

$$\xi = \frac{2\alpha^2}{45m^4} \propto \frac{\alpha}{E_{\mathrm{crit}}^2} \tag{2}$$

with α being the fine structure constant, m the particle's rest mass (those constituting the virtual pairs), and E_{crit}^2 the critical field of QED. Considering electrons and positrons as lightest and therefore most relevant species (due to $\propto m^{-4}$-scaling) for the quantum fluctuations, the critical field in SI units is

$$E_{\mathrm{crit}} \approx 1.3\cdot 10^{18}\,\mathrm{V\,m^{-1}} \tag{3a}$$
$$B_{\mathrm{crit}} = E_{\mathrm{crit}}/c \approx 4.4\cdot 10^{9}\,\mathrm{T} \tag{3b}$$
$$I_{\mathrm{crit}} \approx 4.4\cdot 10^{29}\,\mathrm{W/cm^2} \tag{3c}$$

where c the vacuum speed of light. This relation shows the magnitudes the fields must have such that those effects occur. Nuclei of atoms provide very strong Coulomb fields and lead to specific QED corrections, referred to as Lamb shift, Anomalous magnetic moment and Delbrück scattering[22–28].

More attractive to scientists is the case of controllable fields, i.e. laboratory vacuum and laboratory fields. The reason for the interest is the dependence on m^{-4}, such that hypothetical light particles would contribute significantly.

Considering two different origins of the fields, a strong background field and a weak probing field, the right part of Eq. (1) describes a correction Δn of the refractive index to the classical $n = 1$ for vacuum. Yet, depending on the relative k-vector and electric field orientation, there are *two components* for left- and right-handed circular polarization components of the probe field like

$$n_{\pm} = 1 + (11 \pm 3)\xi E_{\mathrm{crit}}^2 \times \mathcal{A} \tag{4}$$

with $\mathcal{A}$ being a measure of quadratic field strength normalized to the critical field, like $(E/E_{\mathrm{crit}})^2$ or $(B/B_{\mathrm{crit}})^2$ for static fields or I/I_{crit} for a beam intensity I, see Sec. 3.

Hence, the difference of the phase velocities yields a birefringence of vacuum[17–19,29–36] whereas the difference from $n = 1$ yields a refraction in general. Furthermore, the external field, polarizing the vacuum, can be realized by static fields or by electromagnetic waves. The latter is considered photon-photon or light-by-light scattering[37,38] which would not happen in classical electrodynamics. A good overview of vacuum birefringence is given in the recent review article[39] and references therein.

So far, vacuum birefringence laboratory experiments employ linearly polarized optical laser beams in magnetic fields and are reported for PVLAS[40,41], BMV[42] and Q&A[43,44] . Ejlli *et al.*[41] concluded the final limits on vacuum magnetic birefringence Δn and dichroism $\Delta\kappa$ of the PVLAS-FE experiment at $B = 2.5\,\mathrm{T} \approx 5.7\cdot 10^{-10} B_{\mathrm{crit}}$ are

$$\Delta n = (12 \pm 17)\cdot 10^{-23} \text{ and}$$
$$\Delta\kappa = (10 \pm 28)\cdot 10^{-23} ,$$

respectively. The experiment is compatible with the absence of vacuum birefringence. Agil *et al.*[42] clarify that the limiting noise affecting the vacuum linear magnetic birefringence experiment is a birefringence one, and expect to get 100 times better results in polarimetry experiments by eliminating the limiting noise in BMV experiment.

The major challenge of vacuum birefringence experiments is the extremely small effect, where two laboratory quantities may leverage: A) the provision of sufficiently strong external fields by intense radiation and B) using a shorter probe wavelength. The former argument is pretty clear when considering Eq. (4) and $\mathcal{A}$. The latter argument is derived from the phase shift being the observable for changes of the refractive index: for a birefringent medium of length ℓ, the accumulated phase shift is $\Delta\phi = 2\pi\cdot\Delta n\cdot\ell/\lambda$, with λ being the wavelength of the probe beam passing through the birefringent vacuum.

For the above-mentioned studies, the effective path is generated by a Fabry-Perot-setup in meter-long magnetic fields, providing $\ell \sim 10^6\,\mathrm{m}$ while $\lambda \sim 10^{-6}\,\mathrm{m}$, thus $\ell/\lambda \sim 10^{12}$. However, $\mathcal{A} \sim (10^{-10})^2 = 10^{-20}$. In contrast, schemes proposing an intense laser beam to generate the birefringence and an X-ray beam for probing

https://doi.org/10.1017/hpl.2023.45 Published online by Cambridge University Press

gain significantly by the field strength but loose in effective interaction length: $\mathcal{A} = I/I_{\rm crit} \sim 10^{21}/10^{29} \sim 10^{-8} \ggg 10^{-20}$ and $\ell/\lambda \sim 10^{-6}\,{\rm m}/10^{-10}\,{\rm m} \sim 10^{4} \ll 10^{12}$ can be estimated. Comparing the schemes, the latter promises a factor $10^{-8}/10^{-20} \cdot 10^{4}/10^{12} \sim 10^{4}$ more phase shift than the current laboratory experiments.

This stimulated scientists to improve the performance of X-ray polarimetry. Here, we review the related studies. In this paper, the contents are as follows: we introduce X-ray polarimetry in Section 2. First of all, we discuss the polarization purity of X-rays and the influencing factors and limitations in Section 2.1, followed by details for high-quality X-ray polarizer in Section 2.2. In Section 3, we present the details of detecting vacuum birefringence, including experimental setups (Section 3.2) and general signal estimates (Section 3.3). We further discuss available facilities (Sec. 3.4) and related instrumentation (Sec. 3.4.4). Section 4 is a brief description of applications of X-ray polarimetry to nuclear resonant scattering, strong field physics and astrophysics.

2. X-ray polarimetry

The basic schematics shown in Figure 1 can be transferred to the X-ray domain, such that polarizing elements are required for the roles of polarizer and analyzer. Here we discuss the crucial components and potential accuracy of X-ray polarimetry. At first, we would like to introduce two methods to obtain polarized X-rays.

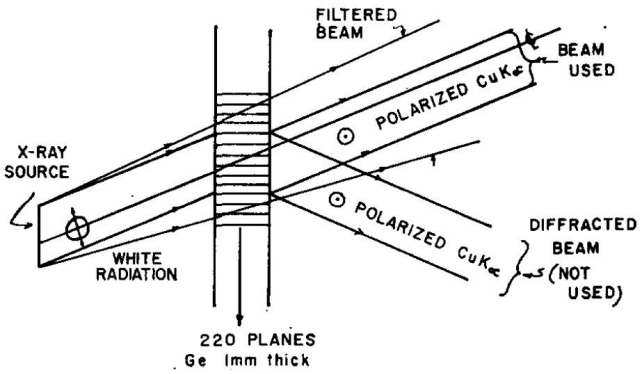

Figure 2: Basic diffraction geometry for anomalous transmission of X-rays (Borrmann effect). Taken from Cole *et al.*[45].

The Borrmann effect, or anomalous transmission, was discovered by Borrmann[46] in 1941. The polarized X-rays are produced when X-rays pass through crystals because of the *different absorbance* of two orthogonal polarization planes[45,47]. The polarization state with the electric vector in the plane of incidence is preferentially absorbed, in comparison to the polarization state with the electric vector perpendicular to the plane of incidence. Here, the polarizers based on the Borrmann effect are applied to the investigation of electric-magnetic properties of ferroelectric materials and optical properties in chiral compounds[16,48]. The drawbacks of this polarizer are low efficiency and a narrow angular acceptance[49]. In 1961, Cole[45] *et al.* constructed a polarizer-monochromator, where the polarizer is made from a single Germanium crystal slab with $1\,{\rm mm}$ thickness, and the diffracted beam based on Borrmann effect is polarized, as shown in Figure 2. The best intensity ratio of the two orthogonal polarization states based on Borrmann effect is less than $1.5 \cdot 10^{-5}$ for a $2\,{\rm mm}$ thick Silicon crystal polarizer and $4\,{\rm mm}$ thick analyzer[48].

Alternatively, polarized X-rays can be produced on perfect crystals with the Bragg diffraction at nearly 45° and thereby exploiting *Brewster's law*[10,50]. As shown in Figure 3, the Bragg diffraction happens near the crystal surface for low absorption. The polarization component parallel to the plane of diffraction ($\parallel$ state or π or p-polarization state) disappears due to Brewster's law, but the vertical polarization component ($\perp$ state or σ or s-polarization state) remains. In this way, linearly polarized X-rays are generated. Disadvantages are the requirement of exactly 45° Bragg angle and the limitation of wavelengths due to materials.

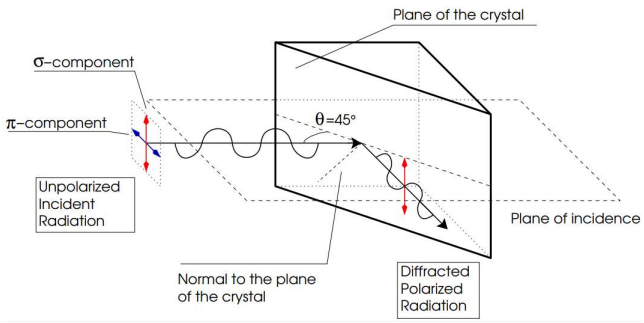

Figure 3: Geometry of the Bragg diffraction at 45 degrees. Unpolarized radiation is polarized because the π-component, being in the plane of incidence, is not allowed for reflection (Brewster's law). Taken from Muleri *et al.*[50].

2.1. Polarization purity

Here we discuss the generation of pure linear polarization states of X-rays based on Bragg diffraction at perfect crystals[51–54]. The polarization purity $\mathcal{P}$ is defined as the intensity ratio of the (suppressed) polarization π-component to σ–component, as shown in Figure 3, and then integrated over angle θ and wavelength λ ranges[52,54]:

$$\mathcal{P} = \frac{\int\int I_\pi(\lambda,\theta)\,{\rm d}\lambda\,{\rm d}\theta}{\int\int I_\sigma(\lambda,\theta)\,{\rm d}\lambda\,{\rm d}\theta} \tag{5}$$

Obviously $0 < \mathcal{P} \leq 1$, and a high degree of linear polarization means $\mathcal{P} \ll 1$. Thus $\mathcal{P}$ is a measure of relative impurity. On the other hand, for a perfectly polarized source with N photons and a polarization-independent transmission

https://doi.org/10.1017/hpl.2023.45 Published online by Cambridge University Press

T of the polarizer, $NT\mathcal{P}$ photons are transmitted in a crossed polarizer setting.

The intensity ratio of the polarization components σ to π is related with the integrated reflectivity of two polarization states, R_σ and R_π, over angle as

$$\frac{I_\pi}{I_\sigma} = \frac{\int R_\pi(\theta)\ \mathrm{d}\theta}{\int R_\sigma(\theta)\ \mathrm{d}\theta}\ . \tag{6}$$

In the following we discuss the requirements and limitations of extreme high purities $\mathcal{P} \ll 1$.

2.1.1. Beam divergence As very simple geometric effect, a beam divergence leads to a deviation from exactly $45°$ Bragg angle for some parts of a beam, impinging on a perfect crystal, and thus a minor contribution into the π-polarized component[52]. Assuming the X-ray beam is a Gaussian beam, the relationship between the divergence and the polarization purity is[52,55]

$$\mathcal{P}^{\text{Limit}}_{\text{Divergence}} = \sigma_{\text{H}}^2 + \sigma_{\text{V}}^2 \tag{7}$$

with σ_{V} and σ_{H} being the divergence in the vertical and horizontal direction, respectively.

σ_H	$\mathcal{P}_{\text{exp}}$	$\mathcal{P}^{\text{Limit}}_{\text{Divergence}}$
$17\,\mu\text{rad}$	$(3.3 \pm 0.7) \cdot 10^{-10}$	$3.2 \cdot 10^{-10}$
$14\,\mu\text{rad}$	$(2.2 \pm 0.9) \cdot 10^{-10}$	$2.3 \cdot 10^{-10}$
$8.4\,\mu\text{rad}$	$(1.4 \pm 0.5) \cdot 10^{-10}$	$1.1 \cdot 10^{-10}$

Table 1: Taken from Bernhardt *et al.*[55]: Comparison of measured purity $\mathcal{P}_{\text{exp}}$ against the calculated limit $\mathcal{P}^{\text{Limit}}_{\text{Divergence}}$ given by the beam divergence σ_H for $\sigma_V = 6.1\,\mu\text{rad}$.

In 2020, Bernhardt *et al.*[55] experimentally verified Schulze's[52] theoretical analysis by studying the effect of beam horizontal divergence on X-ray polarization purity at beamline ID18 of the European Synchrotron Radiation Facility (ESRF). The comparison of the X-ray polarization purity between the fitted data ($\mathcal{P}_{\text{exp}}$) and the calculated data ($\mathcal{P}^{\text{Limit}}_{\text{Divergence}}$, using Eq. (7)) is presented in Table 1. The polarization purity from the fitted data points and the calculated limit match very well for all three horizontal beam divergences. When the horizontal divergence of X-ray was reduced from $17\,\mu\text{rad}$ to $8.4\,\mu\text{rad}$ by a slit with variable gap and a V-shaped channel-cut (VCC), the X-ray polarization purity decreased to $1.4 \cdot 10^{-10}$[55]. In addition, this paper and others[19,56] mention that $1\,\mu\text{rad}$ divergence is available for the XFEL. Therefore, the X-ray polarization purity is limited to the order of 10^{-12}.

2.1.2. Crystal quality Crystal quality affects the polarization purity in two ways. First, for similar geometric reasons as the divergence, all parts of a (perfectly parallel) beam of finite size must experience the same $45°$ incidence angle to allow for same polarization suppression[54]. Secondly, imperfect crystals have varying lattice constants which affect the reflectivity curves and thus the spectral/angular acceptance and integrated reflectivity. Thus, the properties of the crystal material must be taken into account to avoid the depolarization of X-rays.

Researchers[53,55] used artificial diamonds containing a mass of crystalline defects produced by chemical vapor deposition (CVD) as a polarizer in X-ray polarimetry. Contrary to expectations and the prediction of Hart and Rodriguez[54], imperfections of artificial diamonds have no observable influence on the polarization purity of X-ray but lead to low peak reflectivity and low transmittance of polarizers[55]. Furthermore, polarimetry at photon energies above $10\,\text{keV}$ can benefit from imperfections because of the higher integrated reflectivity. For low photon energies, the nearly perfect crystals with high reflectivity are essential for the expected highly linearly polarized X-ray[55].

2.1.3. Detour reflections (Umweganregungen) Another limitation of the polarization purity are detour reflections (Umweganregung)[57]. Those are the result of consecutive Bragg diffractions on different lattice planes and therefore different Bragg angles, yielding in sequence the same beam reflection angle as the primary reflection. This is similar to a cat's-eye retro-reflector, where the rays bounce of several surfaces, in contrast to a mirror where only one reflection occurs. In fact, the detours are only possible in 3D crystals due to the abundance of lattice planes in directions off the main reflection.

As result, every partial Bragg diffraction does not happen with $45°$ Bragg angle such that the Brewster condition is not fulfilled, and no strong ratios of $R_\pi : R_\sigma$ are yielded, even in sequence. Yet, the overall intensity can be relatively weak compared to the beam from the $45°$ (main) Bragg diffraction. Still, these unpolarized contributions yield a limit for the polarization purity.

The Ewald sphere is a geometric construction to determine the diffraction direction of crystal, and diffraction will occur only for reciprocal lattice points that lie on the surface of the Ewald sphere. The consecutive reflections case happens at nearby lattice planes in 3D crystals if there are more than two reciprocal lattice points which lie on the Ewald sphere. Under some azimuth angles, the incident beam excites not only the required intended reflection with $45°$ Bragg angle but also secondary reflections – not with $45°$ Bragg angle. As a result, the latter reflections will cause the depolarization of X-rays when the secondary, detoured reflections exit into the same exit direction of the principal reflection[51,53,57], and the polarization purity is suppressed. Marx *et al.*[51] displayed the reflection system for a silicon crystal and an X-ray energy of $12.914\,\text{keV}$ in Figure 4. The radius of the Ewald sphere is $1/\lambda$, where λ is the wavelength of the

https://doi.org/10.1017/hpl.2023.45 Published online by Cambridge University Press

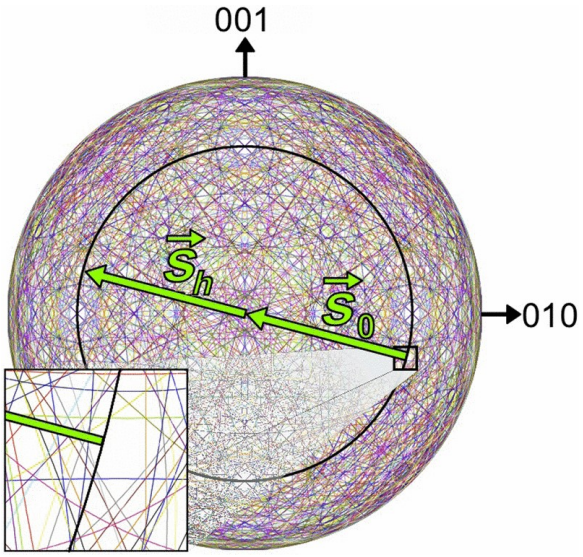

Figure 4: Kossel pattern of silicon at $12.914\,\mathrm{keV}$. The bold black circle represents the exploited Si (800) reflection used for suppression of the component. All other possible reflections are depicted by thin colored circles. The vectors $\vec{S}_0$ and $\vec{S}_h$ describe the direction of the incident and diffracted wave respectively. In order to avoid degradation of the polarization purity due to multiple-beam cases, the azimuth has to be chosen such that the "distance" to the closest undesired reflections is as large as possible. Taken from Marx *et al.*[51].

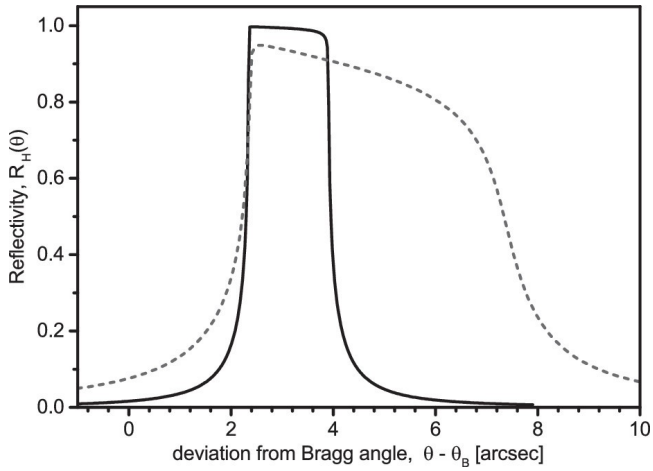

Figure 5: Reflectivity of X-rays for the σ–polarization in $45°$ symmetric Bragg scattering geometry as a function of the angle of incidence, according to dynamical theory calculations. Solid line: the (400) Bragg reflection in diamond for $9.831\,\mathrm{keV}$. Dashed line: the (400) Bragg reflection in Silicon for $6.457\,\mathrm{keV}$, as used by Marx *et al.*[51]. Taken from Bernhardt *et al.*[53]. Note that $1'' \approx 5\,\mu\mathrm{rad}$.

incident beam. The intersections of the color lines are the multi-beam cases. The effect of multi-beam situations can be reduced by optimizing the crystal azimuth to avoid the excitation of secondary reflections[53]. In addition, using lower photon energies reduces the size of the Ewald sphere and therefore reduces the number of potential detour cases.

2.1.4. Material dependence It is obvious from the previous sections that the material has a strong influence, mainly to provide crystals of highest quality, cf. Sec. 2.1.2. At present, Si ($Z = 14$)[51,58–60] and diamond ($Z = 6$)[53,55] are widely available. Ge ($Z = 32$)[61] exhibits a reflection for Cu X-ray tubes but is abandoned gradually. Silicon crystals with perfect crystal structure, few impurities and a very mature preparation technology are adopted widely as polarizer.

For silicon and diamond, Bernhardt *et al.*[53] compare the reflectivity of those two materials of the Bragg reflection at $45°$ angle as illustrated in Figure 5. The solid line and dashed line are the reflectivity curves of diamond and silicon, respectively. The curve for diamond is higher but narrower than that for silicon. That is a quite general behaviour[62] and the reason lies mainly in the number of electrons per atom, Z. Silicon has more electrons, thus scatters more intensity per lattice plane, and less lattice planes are needed for Bragg reflection. That explains the wider spectral/angular width of the curve. On the other hand, the absorption per atom of silicon is higher, thus the peak reflectivity is not as high as for diamond. The photon energy E_{ph} also plays a role here, as diamond has a smaller unit cell and thus the wavelength for the same (400) reflection is shorter. With higher photon energy, absorption reduces and penetration increases, hence this also contributes to the narrower and higher curve of diamond.

For applications, however, the integrated reflectivity can be of interest, e.g. if the beam has a finite spectral bandwidth or divergence. The integrated reflectivity of diamond is much smaller than that of Silicon. For example, a later work by Bernhardt *et al.*[55] used diamonds with plenty crystalline defects and showed a peak reflectivity of only 50 %-60 % while the rocking curve broadened by a factor ~ 2.

There is also a material dependence of detour reflections. Tischler *et al.*[63] provide that the resulting contribution of all reflections is dependent on the amplitude for each detour:

$$E_{\mathrm{mult}} = \sum_{i=1}^{N} E_i. \tag{8}$$

Based on Eq. 8, they calculated the N-beam integrated intensities for the (622) reflection of Germanium (Ge) and Silicon (Si). The ratio of intensities is very close to the ratio of atomic numbers to forth power[51,55,58,59]:

$$\left(\frac{E^{\mathrm{Ge}}_{\mathrm{mult}}}{E^{\mathrm{Si}}_{\mathrm{mult}}}\right)^2 = \left(\frac{0.038}{0.0075}\right)^2 \simeq 25.7 \approx \left(\frac{Z_{\mathrm{Ge}}}{Z\mathrm{Si}}\right)^4 = \left(\frac{32}{14}\right) \simeq 27.3\ .$$

https://doi.org/10.1017/hpl.2023.45 Published online by Cambridge University Press

Consequently, polarizers made by material with low Z value are favorable to further mitigate the impact of detour reflections, apart from chosing a good azimuth angle.

2.2. Channel-cut precision X-ray polarizers

The significant optical element in X-ray polarimetry for high polarization purity is the polarizer. In 1978 and 1979, Hart *et al.*[11,54] established an X-ray polarimetry with two-fold Bragg-reflecting channel-cut germanium (Ge) crystals and pointed out that the polarization with multiple Bragg reflections has been demonstrated for any X-ray wavelength by using offset grooved crystals. Figure 6 displays a channel-cut polarizer with 4 reflections at 45° Bragg angle.

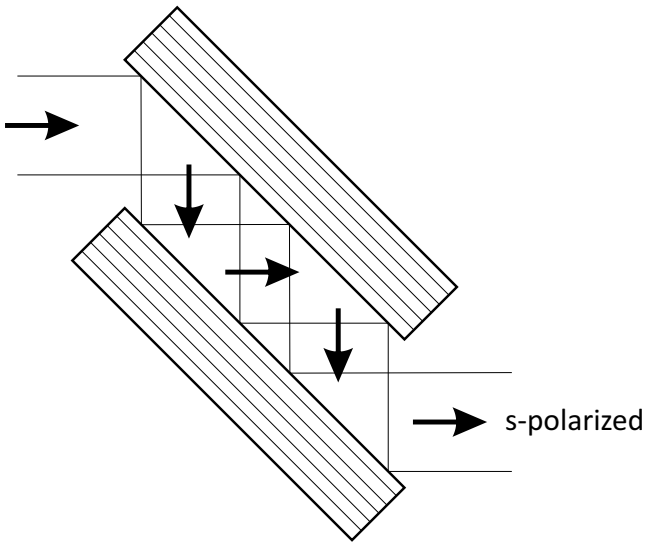

Figure 6: Schematics of a channel-cut polarizer with 2×2 reflections. Thin lines indicate the lattice planes for the 45° Bragg reflection, which are parallel to the surface in this case.

As can be seen in Figure 6, it consists of two opposing Bragg crystals for 45° Bragg angle. For simplicity and convenience, the two surfaces are made from a single crystal with a groove or channel cut into it. Thereby, the two surfaces have naturally parallel lattice planes. With appropriate geometry, an even number of reflections can be obtained, maintaining the beam direction while improving the purity (see below Sec. 2.2.1). The resulting parallel offset of the beam is a minor problem. The main advantage is the inherent parallelism of both (opposing) lattice planes, such that the Bragg angle is to be aligned only once for all occurring reflections.

One method to machine grooves is lapping by low-damage blades of a crystal saw. Alternatively, etching technologies are also excellent to have near-perfect inner channel surfaces to avoid distortions of the X-ray wavefront[58,59]. Channel-cut crystals have extensive use[51–54,64]. As early as 1965, Bonse and Hart[64] pointed that the pairs of perfect crystals with groove cut (Figure 6) obviously reduced the tails caused by the multiple reflections. In 1978, Hart[11] constructed an X-ray polarimeter with two-fold Bragg-reflecting channel-cut germanium crystals to generate elliptically polarized X-rays. They used a mixture of nitric acid and hydrofluoric acid to polish the channel-cut crystals and eliminate the strains introduced in the cutting process. For channel-cut crystals designs, Marx-Glowna *et al.*[60] pointed out that the calculation of the beam path of Compton scattered photons and the orientation of crystal should be considered, which effects on the polarization purity of X-ray.

2.2.1. Consecutive reflections It is well known that a polarized light beam can be produced by several transmissions through a number of glass plates, even though each plate is only a partial polarizer. Similarly, channel-cut crystals improve the polarization purity[54,65] since they stack a number of reflections into a single optical element.

Regarding multiple successive Bragg reflections between the walls of channel-cut in an ideal crystal to increase the polarization purity of X-rays, the ratio of intensities of two polarization states for X-rays polarized by m consecutive Bragg reflections is given by[66]

$$\frac{I_\pi}{I_\sigma} = \frac{\int R_\pi^m(\theta)\, d\theta}{\int R_\sigma^m(\theta)\, d\theta} \tag{9}$$

with the notations of Eq. (6). Hart[54] calculated the ratio of I_π : I_σ for multiple Bragg reflections in a grooved Ge polarizer using two-beam dynamical theory, shown in Figure 7. The polarization purity decreases as the number of multiple Bragg reflections increases. In 1965, Bonse and Hart[64] analyzed that multiple Bragg reflections between the walls of a channel-cut perfect crystal do not narrow the reflection curves considerably.

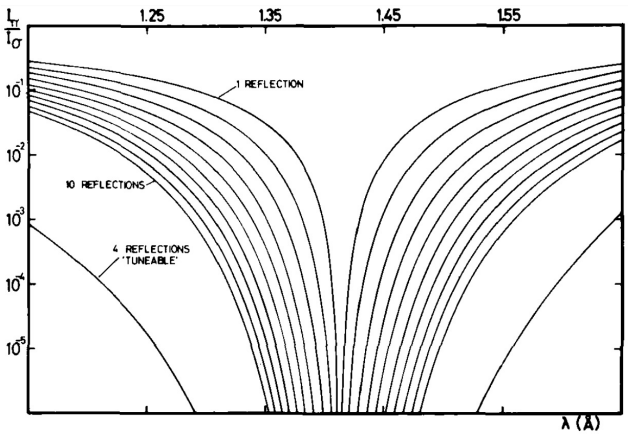

Figure 7: Polarization ratios for m-fold multiple-Bragg-reflection polarizers using the Ge (440) Bragg reflection. Taken from Hart *et al.*[54].

Recently, high polarization purity of X-rays was achieved

https://doi.org/10.1017/hpl.2023.45 Published online by Cambridge University Press

by multiple reflections. In 2011, Marx *et al.*[58] reported that the highest purity of polarization of X-rays reaches to $1.5 \cdot 10^{-9}$ based on $m = 4$ reflections at Si (400) channel-cut crystals at 6 keV X-ray energy. Two years later[51], they obtained $2.4 \cdot 10^{-10}$ polarization purity of the X-ray using $m = 6$ reflections. Here, the energy of X-ray is 6 keV and the polarizer is Si (400) channel-cut crystals, same as before.

2.2.2. Asymmetric cuts The channel-cut crystals enhance the polarization purity of X-rays. However, the angular and spectral acceptance of channel-cut crystals tend to restrict the throughput of X-rays. To increase the acceptance of channel-cut crystals while maintaining the polarization filtering, researchers[66–68] came up with asymmetrically cut crystals with an asymmetry angle α_c between the lattice planes and the surface. To quantify the asymmetry, the asymmetry parameter b for a Bragg diffraction is defined[68] by

$$b = \frac{\sin(\theta_\mathrm{B} + \alpha_c)}{\sin(\theta_\mathrm{B} - \alpha_c)} \,. \tag{10}$$

Note that the asymmetry angle α_c is negative if the incidence angle relative to the crystal surface is smaller than exit angle, as for the first reflection shown in Fig. 8.

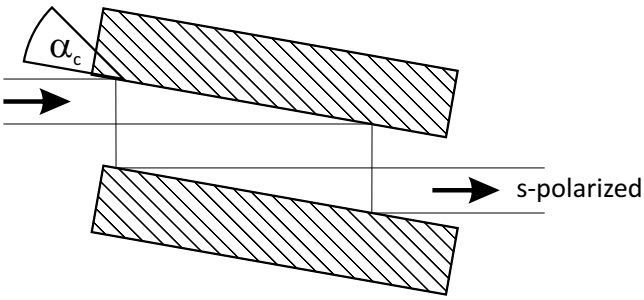

Figure 8: The geometry for an asymmetrically cut channel-cut crystal with a Bragg angle near 45°. The lattice planes, indicated like in Fig. 6, are oriented 45° to the beam, yet the crystal surface is slanted. The asymmetry angle α_c is the angle between surface and lattice planes. It is negative for the case shown at the first surface where the incident beam is shallow and leaves with larger diameter.

The angular acceptance of the crystal varies with asymmetry angle as

$$(\Delta\theta)_\mathrm{asymm} = \sqrt{b} \cdot (\Delta\theta)_\mathrm{symm} \tag{11}$$

with $(\Delta\theta)_\mathrm{symm}$ being the usual acceptance from a symmetric reflection.

Figure 9 displays the effects of asymmetry angle on angular acceptance and polarization suppression[67]. The angular acceptance increases while the polarization suppression factor decreases when the asymmetry angle approaches 45°. However, a larger asymmetry angle requires larger crystals due to beam footprint, imposing practical issues.

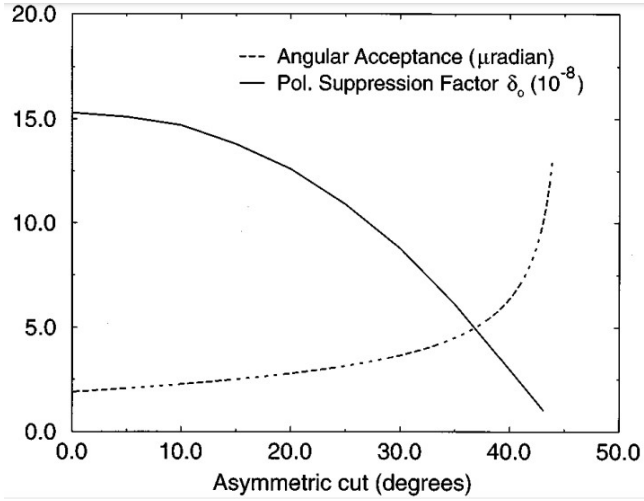

Figure 9: The effect of an asymmetric cutting angle on both the angular acceptance and the resulting polarization suppression for a Silicon (840) channel-cut crystal. Taken from Toellner *et al.*[67].

An overview of calculated polarization purities of X-rays for different asymmetry angles α_c and number of channel-cut reflections m is listed in Table 2 with the explanation of each parameter by annotations. For a same number of reflections, the polarization purity at an asymmetry angle of $-28°$ is better than that of at an asymmetry angle of $-43°$. In the paper, Marx-Glowna[68] chooses $-28°$ asymmetry angle and four reflections because of the practical limitation of crystal size and preparation (high-quality surface), and obtained experimentally $(2.2 \pm 2.0) \cdot 10^{-9}$ polarization purity finally.

α_c [°]	n	D_- [μrad]	S_+ [mm]	I/I_0	$\mathcal{P}$
0	1	1.9	2.5	0.95	$1.1 \cdot 10^{-4}$
0	2	1.9	2.5	0.90	$1.6 \cdot 10^{-7}$
0	4	1.9	2.5	0.81	$5.4 \cdot 10^{-13}$
-28	1	3.4	8.1	0.93	$9.2 \cdot 10^{-5}$
-28	2	3.4	8.1	0.87	$1.1 \cdot 10^{-7}$
-28	4	3.4	8.1	0.76	$2.5 \cdot 10^{-13}$
-43	1	9.9	68.1	0.83	$4.5 \cdot 10^{-5}$
-43	2	9.9	68.1	0.68	$1.1 \cdot 10^{-8}$

Table 2: Taken from Marx-Glowna *et al.*[68]: Calculated polarization purity $\mathcal{P}$ for asymmetry angle α_c and number of reflections n. D_- is the accepted beam divergence, S_+ the beam footprint on the crystal surface and I/I_0 the peak reflectivity.

2.2.3. Quasi-Channel-cuts It may be necessary to realize the two opposing surfaces by two separate crystals. This is called quasi-channel-cut. It may help to tune the Bragg

https://doi.org/10.1017/hpl.2023.45 Published online by Cambridge University Press

	2011 [58]	2013 [51]	2015 [60]	2016 [53]	2020 [55]	2021 [68]	2022 [59]	2022 [72]
Facility	ESRF	ESRF	Petra III	ESRF	ESRF	Petra III	Eu. XFEL	Petra III
Beamline	ID06	ID06	P01	ID06	ID18	P01	HED	P01
E_{ph} [keV]	6.457	6.457	12.914	9.839	9.83	14.41	6.457	12.914
Material	Silicon	Silicon	Silicon	Diamond	Diamond	Silicon	Silicon	Silicon
Reflection	(400)	(400)	(800)	(400)	(400)	(840)	(400)	(800)
m	4	6	6	2	4	4	6	4
α_c	0	0	0	0	0	$-28°$	0	0
σ_H [µrad]	-	10.3	-	10	8.4	-	0.273	18.8
σ_V [µrad]	-	2.9	-	-	6.1	-	≈ 0	25.9
$\mathcal{P}$	$1.5 \cdot 10^{-9}$	$2.3 \cdot 10^{-10}$	$2 \cdot 10^{-9}$	$8.9 \cdot 10^{-10}$	$1.1 \cdot 10^{-10}$	$2.2 \cdot 10^{-9}$	$8 \cdot 10^{-11}$	$1.4 \cdot 10^{-11}$
$\mathcal{P}^{\text{Limit}}_{\text{Divergence}}$	-	$1.2 \cdot 10^{-10}$	-	$1.0 \cdot 10^{-10}$	$1.1 \cdot 10^{-10}$	-	$7.5 \cdot 10^{-14}$	$<10^{-9}$

Table 3: Timeline of precision X-ray polarimetry. m denotes the number of reflections per channel-cut crystal, σ_H and σ_V the beam divergence, and $\mathcal{P}$ the obtained polarization purity. $\mathcal{P}^{\text{Limit}}_{\text{Divergence}}$ is calculated from the divergence according to Eq. (7). For the current record [72], the nominal instrument's beam divergence was reduced by slits at the polarimeter.

reflections separately by an angle offset [54] since the reflectivity curves for both polarizations R_σ and R_π can have different widths and positions in angle.

Furthermore, not all materials can be grown as large bulk as is done for silicon. For example, diamond is quite attractive because of its high thermal conductivity and low absorption in the X-ray region [55], but it is very challenging produce at large sizes and to obtain high-quality diamond with few dislocations and stacking faults. A reflectivity as high as 99 % of hard X-rays from nearly defect-free diamond crystals at near-normal incidence is reported [69]. Nevertheless, low crystal quality and complicated production processes constrain the development of diamond in polarizers. Polarization purities of $8.9 \cdot 10^{-10}$ [53] and $3 \cdot 10^{-10}$ [55] are reported for using artificial diamond crystals manufactured by chemical vapor deposition (CVD).

Technically, the setup is challenging to provide sufficient angular stability of both surfaces.

2.2.4. Temporal effects Another feature, relevant for applications at XFELs in particular, is the inherent pulse stretching effect for Bragg crystals [70,71]. Due to the scattering at the lattice planes happening over many lattice planes (leading to the finite spectral bandwidth), a short X-ray pulse will become temporally stretched. The ray will enter the crystal a certain depth where it is effectively diffracted out, being the Bragg-case extinction depth e. For a symmetric reflection, the projection of penetration will add to the pulse envelope [71] as

$$\Delta\tau = 2e \sin\theta_\mathrm{B}/c\,. \tag{12}$$

This effect increases obviously with the Bragg angle, the number of consecutive reflections, as well as photon energy and material. The latter dependency is not straightforward. Higher photon energy usually leads to deeper penetration, but higher Z of the material leads to stronger diffraction per lattice plane and hence reduced penetration.

2.3. Interim summary

In this chapter, we elaborated on the factors influencing the polarization purity of X-rays in X-ray polarimetry. For high polarization purity of X-rays, the requirements on the polarizer are four-fold: channel-cut crystal, made of high-quality material, multiple Bragg reflections $m = 4$, $m = 6$ or more, and avoiding detour reflections by azimuth angle tuning and material with low Z.

For applications, not only purity $\mathcal{P}$ but also the integrated transmission T may play a role. This can fall back to the choice of m, to considering an appropriate asymmetry angle α_c of the channel-cut or even to a different material due to the Z dependence.

In 2022, Schulze *et al.* [59] reported an unprecedented purity of linear polarization of X-rays at the High Energy Density (HED) instrument of the European XFEL of $\mathcal{P} = 8 \cdot 10^{-11}$, provided by silicon channel-cuts. They calculated the theoretical limitation of polarization purity is $7 \cdot 10^{-14}$ by Eq. (7) with the horizontal divergence of $0.27\,\mu\mathrm{rad}$ and a negligible vertical divergence. This emphasizes the importance of XFELs for further polarizer developments since only XFELs can provide those low divergence beams.

On the contrary, the polarization purity could not be determined better due to limited photon flux and integration time, since the XFEL was operated in SASE mode with large spectral bandwidth, not matched with the polarizers acceptance. Thus the polarization-independent transmission T was low, leading to $NT\mathcal{P}$ photons arriving per pulse at the detector, being at the noise limit. Asymmetric channel-cuts may help for improving T thanks to Eq. 11 (cf. Fig. 9). However, the gain in spectral/angular acceptance is not very high. For $\alpha_c = -43°$, i.e. 2° incidence onto the surface, the acceptance has increased by a factor ∼5 while the beam footprint has increased by a factor ∼27, requiring much

https://doi.org/10.1017/hpl.2023.45 Published online by Cambridge University Press

larger channel-cut crystals.

3. X-ray polarimetry and vacuum birefringence

Many studies and concepts have been published for strong-field QED in general [39,73] and polarization effects in particular. Borysov *et al.* [74] proposed an indirect way to measure vacuum birefringence via experiments on the photon-polarized nonlinear Breit-Wheeler (NBW) process. Xie [75] reviewed the research progress of the pair production from vacuum in ultra-strong laser fields and investigated the effects of electric field polarizations on the number density of pair production. Koga [76] presented the ultrahigh electric field generated by the interaction of micro-bubbles with ultra-intense laser pulses, which can be used to measure the vacuum polarization via the bending of gamma rays traversing the imploded micro-bubble. Brezin and Itzykson [29] suggested to use a laser beam and X-rays to study the small magnitude of effects predicted by quantum electrodynamics. Correspondingly, X-ray polarimetry with excellent performance is proposed in detecting the vacuum birefringence phenomenon.

Currently, thanks to the development of ultra-intense optical lasers and XFELs, researchers [18–20,30,33,35,36,77,78] proposed to probe characteristics of the QED vacuum. Here, the highly purified linearly polarized XFEL interacts with an intense optical laser in vacuum. The XFEL will change its polarization state from linearly polarized to elliptically-polarized. This state can be detected via "flipped photons" behind a polarizer which is crossed to the original linear polarization and thereby prove the vacuum birefringence.

3.1. Vacuum birefringence in the universe

Before going into details for laboratory studies, intense astrophysical magnetic fields are ideal to explore vacuum birefringence by X-ray polarimetry. Taverna *et al.* [79] calculated the polarization properties of X-ray radiation escaping from a magnetar magnetosphere via Monte Carlo code. By these simulations, they proved that polarimetric measurements are sufficiently sensitive to reveal QED effects due to vacuum polarization, and that X-ray polarimetry is an adequate tool to probe the ultra-strong magnetic fields in magnetars. In 2017, astronomers [80] experimentally proved the predictions of QED vacuum polarization effects via optical polarimetry measurement of isolated neutron stars. They measured the optical polarization degree to be 16.43 ± 5.26 % and the polarization position angle is $145.39° \pm 9.44°$, and claimed that was strong evidence for supporting the presence of the QED vacuum polarization effects. Because those values are too high to be reproduced by models that neglect the QED vacuum polarization effects. However, Capparelli *et al.* [81] challenged this claim and compared the experimental data and theoretical calculations. They concluded that the polarization signal in paper [80] was only a 3σ effect. They estimated the probability ratio of the polarization degree in both hypotheses with and without the birefringence effect, and concluded that a convincing proof of QED birefringence requires a degree of linear polarization exceeding 30 %. In 2018, Caiazzo and Heyl [82] found that X-rays from the accretion disks of black holes have changed their polarization state as the photons travel through the magnetosphere and attributed to the vacuum becoming birefringent in presence of a magnetic field. In 2020, Minami *et al.* [83] reported a new result of the cosmic birefringence angle $\beta = (0.35 \pm 0.14)°$ $(68\% C.L.)$ corresponding to the statistical significance of 2.4σ, and reduced the systematic uncertainty by a factor of 2.

Though cosmic birefringence has been detected, its interpretation requires further models and assumptions but still can be controversial. This provides a solid case to study vacuum birefringence under controlled conditions in laboratories.

3.2. Concepts for vacuum birefringence laboratory studies

Studies which were conducted with static magnetic fields and optical lasers were already introduced in Sec. 1. Those could not identify vacuum birefringence due to insufficient sensitivity. As astrophysical phenomena indicate vacuum birefringence but cannot be controlled, numerous conceptions and schemes of vacuum birefringence detection are published. Some of them, based on X-ray polarimetry, are presented in the following.

3.2.1. PW lasers and XFELs In 2006, Heinzl *et al.* [20] considered a petawatt laser system with 140 fs pulse duration, 150 J pulse energy and 10^{22} $\mathrm{W/cm^2}$ intensity in focal region to induce the vacuum birefringence. The schematic diagram of the experimental setup is depicted in Figure 10. The high-power optical laser pulse is focused by an off-axis parabolic mirror (OAP), and the linearly polarized X-ray laser pulse collides with the optical laser pulse at interaction area. Then, a small ellipticity of the X-ray pulse caused by vacuum birefringence will be detected. The whole process happens in vacuum chamber.

Schlenvoigt *et al.* [19] proposed an experimental scheme (Figure 11) based on European XFEL and high energy density (HED) instrument in conjunction with the Relavitistic Laser at Xfel (ReLaX) laser system being developed by the Helmholtz International Beamline for Extreme Fields (HIBEF). In this figure, the main part is the setup for vacuum birefringence detection. The PW laser is also focused by OAP into interaction area. The propagation of XFEL is worth introducing in detail. Well-collimated XFEL is measured by an intensity monitor (IM) to record the number of X-ray photons. Then, the XFEL becomes a linearly polarized beam with $\mathcal{P} \sim 10^{-11}$ polarization purity after polarizer (Pol). The first compound refractive lenses (CRLs) are used to focus XFEL to the interaction

https://doi.org/10.1017/hpl.2023.45 Published online by Cambridge University Press

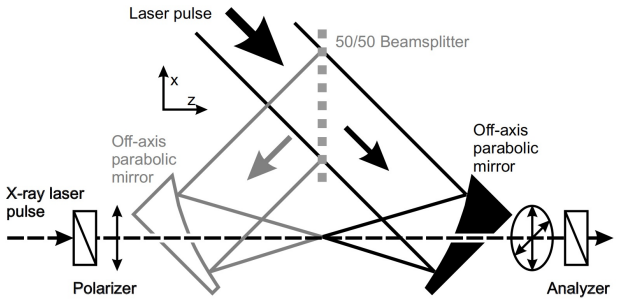

Figure 10: Proposed experimental setup for the demonstration of vacuum birefringence: A high-intensity laser pulse is focused by an F/2.5 off-axis parabolic mirror. A hole is drilled into the parabolic mirror in alignment with the z-axis (axes as indicated) in such a way that an X-ray pulse can propagate along the -axis through the focal region of the high-intensity laser pulse. Using a polarizer-analyzer pair the ellipticity of the X-ray pulse may be detected. Shown in grey: Extension of the setup for the generation of counter propagating laser pulses and a high-intensity standing wave which may be used for pair creation. Taken from Heinzl *et al.* [20]

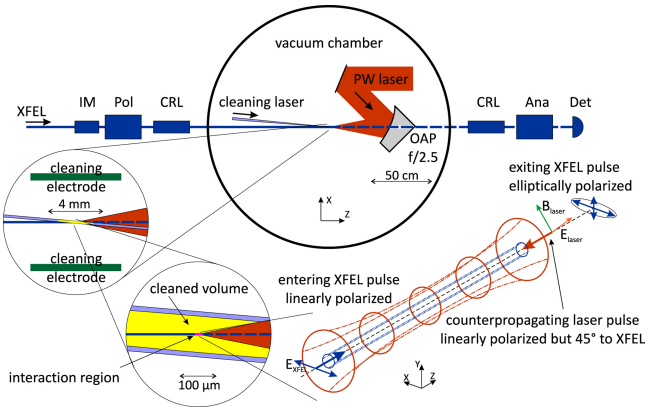

Figure 11: Schematic views of the experimental set-up. Top: a several meter long parts of the X-ray beamline centered around the interaction point with the optical components inside a vacuum chamber. Left: Zoom into a cm sized neighborhood of the focus where the cleaning electrodes will be placed. Bottom left: another zoom into the cleaned region. The focus of the cleaning laser is about 10 μm wide. However, only a fraction (pink) of the cleaned region will be employed as the interaction region, where the PW optical laser ($\sim 2\,\mu$m) and the XFEL beam ($\sim 0.5\,\mu$m) are focused and superimposed. Bottom right: fundamental idea of probing QED vacuum birefringence caused by an intense optical laser with the XFEL beam. Beams are counter-propagating with their foci overlapping in space and time. To maximize the effect, the polarization directions must differ by $45°$. A slight ellipticity in the polarization of the out-going probe pulse will occur. Taken from Schlenvoigt *et al.* [19].

point to overlap with the PW laser focus. The second CRLs are for re-collimation of the X-rays. The analyzer (Ana) is same as Pol in material and geometry but crossed to Pol and only allows photons of flipped polarization to pass, which will be detected by detector (Det). Comparing the photon numbers of initial XFEL pulse and polarization-flipped, vacuum birefringence can be detected.

Moreover, the authors have studied the effect of plasma from residual gas particles on the signal of vacuum birefringence and proposed the method of vacuum cleaning. They plan to introduce another laser called cleaning laser to ionize the gas particles in yellow, named cleaned volume, illustrated in the circle at the bottom left of Figure 11. The cleaned volume is much larger than interaction volume in pink. A static electric field is applied to remove charged particles from the cleaned volume. At the same time, the surrounding gas will repopulate the volume by diffusion, which can be mitigated by correct timing of the cleaning laser pulse. The bottom right is the fundamental idea of probing QED vacuum birefringence by combining XFEL and PW laser.

Subsequently, Shen *et al.* [35,77] presented the experimental design revolving around a 100 PW laser and a 12.914 keV XFEL beam with the station of extreme light at SHINE facility. According to the parameters of the 100 PW laser and adopting the analysis of Schlenvoigt *et al.* [19], the ellipticity is about $2 \cdot 10^{-10}$ and about 170 photons with flipped polarization should be produced by vacuum birefringence if the total photon number at the interaction would be 10^{12}.

There are further works presenting estimates for laser-XFEL studies, concentrating more on modelling and refined beam geometries [33,84]. They also consider 30 J 30 fs 1 PW laser systems in conjunction with 10^{12} probe photons. Recently, Mosman and Karbstein [85] discussed in detail that modelling for ReLaX and European XFEL like Schlenvoigt *et al.* [19] did. However, they used more realistic laser and XFEL parameters, e.g. accelerator setpoint and bunch charge dependency on the number of probe photons, yielding $N \sim 10^{11}$. This number is valid for SASE mode of European XFEL, the spectral matching aspect was published later [59] which effectively reduces the available number of photons. They also discussed XFEL pulse lengthening for channel-cut polarizers, cf. Sec. 2.2.4. Effectively, the polarizer before the interaction will stretch the X-ray pulses to about ~100 fs. This can help for experiments to reduce the temporal jitter effect.

3.2.2. XFEL only The common method of detecting vacuum birefringence is combining the XFEL with a PW-class optical laser. A novel way to detect vacuum birefringence by the collision of two consecutive XFEL pulses under a finite angle has been put forward by Karbstein *et al.* [86]. This idea

https://doi.org/10.1017/hpl.2023.45 Published online by Cambridge University Press

takes the scaling of background field intensity (cf. Sec. 3.3) with wavelength, $I_{\rm BG} \propto \lambda^{-2}$, into account and complements it with the higher repetition rate of XFELs compared to PW-class optical lasers.

Recently, the pulse duration of an XFEL was measured directly[87] to about $\sim$10 fs. This experiments demonstrates that the nonlinear regime of optics may be accessed in the X-ray domain, i.e. sufficiently high photon densities can be produced. With a typical pulse energy of 1 mJ and the aforementioned pulse duration, the XFEL pulse power is about 100 GW. With $\lambda \sim 0.1\,\rm nm$ and further typical beam and focusing parameters ($F_\# \sim 100$), spot sizes below 100 nm are reasonable[88,89], thus focus areas of $\sim 10^{-10}\,\rm cm^2$. As result, intensities of $I_{\rm BG} \sim 10^{20}\,\rm W/cm^2$ can be obtained with XFEL pulses for the background field. That is $\sim 10\,\%$ of optical laser peak intensities. Despite that the ellipticity – being the photon polarization flip probability – scales as $\delta^2 \propto (I_{\rm BG})^2$, the number of flipped photons per unit time (e.g. operating hour) scales with the repetition rate, being easily $10^2 \ldots 10^4$Hz and 1 MHz in future facilties, cf. Table 5. As consequence, the number of flipped photons per unit time can compete with or even exceed the numbers of XFEL-laser combined schemes. Technically, a PW-class laser installation alongside an XFEL is not necessary, but an even more complex X-ray beam path must be realized.

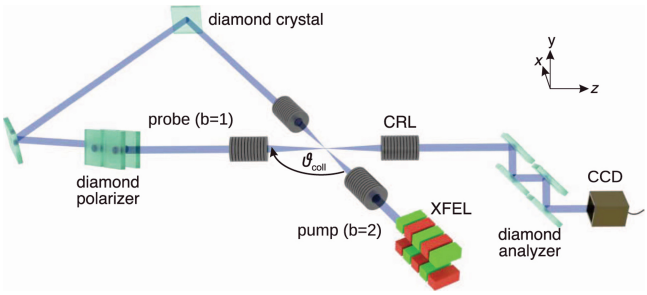

Figure 12: Illustration of the experimental setup utilizing compound refractive lenses (CRLs) to focus and re-collimate the XFEL beam. Reflections at diamond crystals change the propagation direction, and a pair of diamond quasi-channel-cuts serve as polarizer and analyzer, respectively. The original XFEL beam is focused with a CRL to constitute the pump field; the beam focus defines the interaction point. Subsequently, it is defocused with a CRL and by reflection at two diamond crystals directed back to the interaction point under an angle of . Before reaching the interaction point, it is polarized with a diamond polarizer and the resulting probe beam focused to the interaction point with a CRL. Finally, it is defocused with another CRL, analyzed with a diamond analyzer and the signal registered with a CCD. Taken from Karbstein *et al.*[86].

From the installation diagram (Figure 12) we can see, the XFEL beam is focused twice to the interaction region from different directions. This employs the pulse train, such that pulse n is the probe for pulse $n+1$. Along with the beam path, a first set of CRLs generates the pump pulse ($b = 2$), where no high polarization purity is required. Further downstream follows a CRL to recollimate the beam for a delay path, matching the pulse repetition time. Then the XFEL passes through the polarizer made by a channel-cut diamond to become the probe pulse ($b = 1$). They also mentioned the losses and the pulse deformations of XFEL pulse caused by optical elements. In the meantime, each XFEL pulse train should be controlled well to achieve the best possible spatio-temporal overlap of the focused pump and probe beams. Furthermore, each optical element must be of sufficient perfection, for example, the high reflectivity of diamond crystals, and the high perfect focus of CRLs.

Apart from X-ray polarimetry, scientists presented a different approach for measuring vacuum birefringence using multi-MeV to GeV photons[37,90]. King *et al.*[37] did the analytical calculations and numerical simulations for the measurement of vacuum birefrigence by multi-MeV photons, instead of x-ray or optical photons. Nakamiya *et al.*[90] proposed to combine a 10 PW laser system with a 1 GeV gamma-ray photon source to probe the vacuum birefringence effect and designed the γ-ray polarimeter to measure the polarization flip of the probe γ-rays. They derived theoretically the phase retardation of GeV probe photons via pairwise topology of the Bethe-Heitler process in a polarimeter, and concluded it would be possible to observe the vacuum birefringence effect with the accuracy of 4.7 % for the averaged phase retardation $\langle G \rangle$ of 0.72 if 10^4 conversion pairs are available.

3.3. *Estimated ellipticity*

Referring to previous contents, the highly linearly polarized XFEL changes its polarization state to elliptically polarized when it propagates through vacuum which is polarized by focusing a light beam as background field. That is slightly different from the quasi-constant fields employed in studies with optical laser polarimetry, cf. Sec. 1. The calculations lead to similar expressions, such that a difference of refractive index, Eq. (4), leads to a phase shift of two circular polarization components of the linearly polarized XFEL as

$$\Delta\phi = 2\pi \frac{\ell}{\lambda} \Delta n = \frac{4\pi\alpha}{15} \frac{\ell}{\lambda} \frac{I_{\rm BG}}{I_{\rm crit}} \qquad (13)$$

where α is again the fine structure constant, $I_{\rm crit} \approx 4.4 \cdot 10^{29}\,\rm W/cm^2$ the critical intensity derived from Eq. (3), λ the wavelength of the radiation experiencing the vacuum birefringence (here XFEL), $I_{\rm BG}$ the intensity of the background field and ℓ the interaction length. The ellipticity of the XFEL, probing the vacuum birefringence, is

$$\delta^2 = (0.5\Delta\phi)^2. \qquad (14)$$

It must be noted that this effect is maximized if a) the

https://doi.org/10.1017/hpl.2023.45 Published online by Cambridge University Press

background field is counterpropagating to the probing pulse and b) the background field polarization is $45°$ to the probe field polarisation[20,35].

Heinzl *et al.*[20] considered for a Gaussian optical laser beam as background field to set $\ell = z_{\text{Rayleigh, BG}}$. That would be correct if the background field would have no time dependence during the interaction. However, they consider the case of a pulsed laser, either in a counter-propagating way or as standing wave (grey part in Fig. 10. That leads in both variants to a time-dependence, such that the time dependence of the probe must be considered.

Schlenvoigt *et al.*[19] refined the analytical framework of Heinzl by taking their result as differential phase shift and integrated analytically for counter-propagating Gaussian beams with Gaussian pulse shapes, and accounted for temporal and spatial offsets, enabling an analysis for jittering conditions. This approach showed that ℓ can be determined by the geometric pulse length $c \cdot \tau_{\text{BG}}$, but does not yield analytical expressions. In comparison to Heinzl *et al.*, assuming here 2 times higher laser intensity, Schlenvoigt *et al.* estimate a factor 10 less ellipticity due to their more accurate modelling. Mosman *et al.* referred to the same facility but with again reduced laser pulse energy and thus reduced peak intensity ($1/3$ of Schlenvoigt *et al.*) and found a reasonably well down-scaled ellipticity of $3.5 \cdot 10^{-13}$.

In view of considerably differing estimates due to many influencing factors, we only provide scalings[19,85] with the relevant quantities. First we address the background field intensity:

$$I_{\text{BG}} \propto P_{\text{BG}} \propto E_{\text{BG}} \cdot (\tau_{\text{BG}})^{-1} \tag{15a}$$
$$I_{\text{BG}} \propto (w_{\text{BG}})^{-2} \propto (\lambda_{\text{BG}})^{-2} \cdot (F_{\#})^{-2} \tag{15b}$$

where P_{BG}, E_{BG} and τ_{BG} denote the pulse power, pulse energy and pulse duration, respectively, and λ_{BG}, w_{BG} and $F_{\#}$ the wavelength, focus waist and focussing F-number (ratio of focal length to effective beam diameter), respectively. In the next step, the ellipticity scales as

$$\delta^2 \propto (I_{\text{BG}})^2 \tag{16a}$$
$$\delta^2 \propto \lambda^{-2} \tag{16b}$$

with λ again the wavelength of the probing X-ray beam, not the driving optical laser. This again shows the importance of short probe wavelengths and high intensities. However, it must be kept in mind that there can be couplings to ℓ or other parameters, depending on the scheme. E.g. a shorter background pulse duration increase the intensity but reduces the the interaction length ℓ, such that the effect can be quite weak.

The previous equations can be combined and yield, employing for clarity $\hbar\omega_{\text{probe}}$ instead of λ,

$$\delta^2 \propto \frac{E_{\text{BG}}^2 (\hbar\omega_{\text{probe}})^2}{\tau_{\text{BG}}^2 \lambda_{\text{BG}}^4 F_{\#}^4} \,. \tag{17}$$

Reference	Laser power	Intensity W/cm^2	Ellipticity
Heinzl[20]	1 PW	$1 \cdot 10^{22}$	$5 \cdot 10^{-11}$
Schlenvoigt[19]	1 PW	$2 \cdot 10^{22}$	$4 \cdot 10^{-12}$
Shen[35]	100 PW	$2 \cdot 10^{23}$	$2 \cdot 10^{-10}$
Mosman[85]	0.3 PW	$2 \cdot 10^{21}$	$4 \cdot 10^{-13}$

Table 4: Comparison of laser parameters and expected ellipticity (for 13 keV photon energy) of proposed experiments. Note that Heinzl *et al.*[20] did not compute effects of pulse duration and beam shapes, leading to a relatively large ellipticity.

Table 4 summarizes the ellipticity values for the different XFEL-PW proposals discussed in Sec. 3.2.1. Please note that Heinzl *et al.*[20] did employ a rough estimate for beam shapes and interaction length, leading to relatively large estimated ellipticity for a 1 PW laser.

3.4. Readiness review

Regarding the detection of such ellipticity, a polarimeter with crossed polarizations would be realized. The ellipticity is effectively the probability that a probe beam photon flips its polarization state. Therefore, referring back to Sec. 2.1 and considering N photons being emitted at the source and passing through an arrangement with polarization-independent transmission T, $\sim NT\delta^2$ flipped photons would arrive at a detector, whereas $\sim NT\mathcal{P}$ photons would be not flipped but still transmitted towards the detector, being a background[19]. Thus there are 3 challenges for detection:

- large number of photons per pulse N,
- high overall transmission T,
- ellipticity δ^2 competitive with or exceeding purity $\mathcal{P}$.

In addition, such detection would require integration of photons to achieve a certain confidence limit, probably by a number of repetitions m. It was shown[19] that

$$m^{-1} \propto N \cdot T \times \frac{\delta^2}{\mathcal{P}}. \tag{18}$$

The integration time can be reduced by N, T and $\delta^2/\mathcal{P}$ equally. In the following we will address these points.

3.4.1. XFEL facilities XFELs are indispensable sources for structural analysis and contributed to the development of ultra-fast processes. XFEL facilities blossom all over the

https://doi.org/10.1017/hpl.2023.45 Published online by Cambridge University Press

Facility	soft/hard	Beam energy	Photon energy	Repetition rate
FLASH	soft	0.35–1.25 GeV	14–620 keV	4 kHz – 1 MHz
LCLS	both	2.5–16.9 GeV	0.28–28.8 keV	120 Hz
SACLA	hard	5.1–8.5 GeV	4–20 keV	60 Hz
FERMI	soft	1–1.5 GeV	20–310 eV	50 Hz
PAL-XFEL	both	3.5–10 GeV	0.28–20 keV	60 Hz
SwissFEL	soft	2.1–5.8 GeV	250–1,240 keV	100 Hz
European XFEL	both	8.5–17.5 GeV	0.24–25 keV	27 kHz
SXFEL	soft	1–1.6 GeV	124–1,000 eV	50 Hz
LCLS-II (HE)	both	4–15 GeV	0.2–25 keV	120 Hz, 1 MHz
SHINE	both	8 GeV	0.4–25 keV	1 MHz

Table 5: Overview of XFEL facilities. Bold facility names indicate facilities with an ultra-intense laser in operation. Italic are planned facilities. Adapted from Huang *et al.*[91].

world[91] . In Europe, Deutsches Elektronen-Synchrotron (DESY)[92,93], one of accelerator centers, contains three large accelerators: PETRA III, FLASH and European XFEL. FLASH supplies soft X-rays and PETRA III and EuXFEL supply hard X-rays. Italian Elettra Sincrotrone Trieste[94] has two advanced light sources: Elettra and FERMI. The third-generation synchrotron radiation facility Elettra produces synchrotron radiation in wavelength range from infrared to hard X-rays, while FERMI is a seeded free electron laser working in ultraviolet and soft X-ray range. SwissFEL[95,96] is Switzerland's X-ray free-electron laser with hard X-ray FEL with 0.1 nm wavelength and 20 fs pulse duration at Paul Scherrer Institute (PSI).

In the USA, the Linac Coherent Light Source (LCLS)[97,98] at SLAC achieved first lasing and FEL saturation at 0.15 nm in 2009. Its upgrade LCLS-II[99] is designed to produce high-energy X-rays covering the energy range from 200 eV to 1.5 keV for soft X-rays and from 1 keV to 5 keV for hard X-rays. A further upgrade[100] from 4 GeV to 8 GeV beam energy will extend the photon energy range to at least 12.8 keV.

In Asia, the first FEL facility was SPring-8 Ångström Compact Free-Electron Laser (SACLA)[101] in Japan, with a peak X-ray laser power of 1 GW and wavelengths of 0.1 nm. It has matured to multi-beamline, soft and hard X-ray operation[102,103] and extreme intensities[87]. The Pohang Accelerator Laboratory X-ray Free Electron Laser (PAL-XFEL)[76] produces wavelengths of 0.1 nm and 1 nm for hard and soft X-rays, respectively. In China are two facilities[104,105]: the Soft X-ray Free Electron Laser (SXFEL) performs the shortest wavelength of 2 nm, and the Shanghai Hard X-ray Free Electron Laser (SHINE) with 0.05 nm wavelength is being constructed. All those facilities with brilliant X-rays enable scientists in gaining insights into the properties, ultrafast processes and the essences of matter.

We are not discussing synchrotron sources for two reasons. They are currently limited in beam divergence and thus in polarization purity. Furthermore, their pulses are much longer than the background field pulses and contain far fewer photons than XFEL pulses.

In the context of X-ray polarimetry of vacuum birefringence, it must be noted that probe beam photon numbers are often over-estimated in experiment proposals. Typical XFEL pulse energies are of the order of 1 mJ which yields at 12 keV about 10^{11} photons[19]. In addition, the usual spectral bandwidth of XFELs is of the order to 1 % in SASE mode. With self-seeding schemes[106–108], a reduction to 10^{-4} is possible at the cost of reduced pulse energy. This sets requirements on the spectral/angular acceptance of crystal optics like channel-cut crystal polarizers, in particular the widths of Bragg reflectivity curves like shown in Fig. 5.

A relative spectral width of 10^{-4} at $\theta_B = 45°$, matching the self-seeding bandwidth, requires a reflectivity curve width of $10^{-4}\,\mathrm{rad} = 20''$. Thus the dashed curve in Fig. 5, having a width of $\approx 6''$, would have a spectral transmission of ~ 0.3 for self-seeded FEL pulses. Using an asymmetric cut, see Sec. 2.2.2, can increase the reflectivity curve width. As an example, in order to widen the curve by the required factor $\sim$ 3, an asymmetry angle $\alpha_c \sim -40°$ would be necessary. That would increase the beam footprint on the channel-cut crystal surface by ~ 10.

For higher photon energies, e.g. the solid curve in Fig. 5 for $E_{ph} \sim 10\,\mathrm{keV}$, the reflectivity curves become narrower due to deeper penetration. As consequence, improving the bandwidth by the asymmetry angle α_c becomes increasingly impractical.

3.4.2. PW-class laser facilities Ultra-intense pulsed lasers are known to produce the highest light intensities on earth and are thus favorable tools to generate the background field in their focus, polarizing the vacuum helped by a counter-propagating probe light. Table 4 already provided estimated ellipticities for relevant peak intensities. Those intensities are in reach of currently available laser technology. Recently, laser scientists at the Center for Relativistic Laser Science (CoReLS) in Korea reported a peak laser intensity exceeding $10^{23}\,\mathrm{W/cm^2}$[109], generated from a 4 PW laser pulse.

Ultra-intense laser systems are nowadays commercially

https://doi.org/10.1017/hpl.2023.45 Published online by Cambridge University Press

available and are widely employed. They are in general based on the chirped pulse amplification scheme (CPA)[110] and exhibit pulse durations of $\sim$10 fs – $\sim$1 ps, typical wavelengths are 800 nm or 1.05 μm. An overview can be found at "The International Committee on Ultra-High Intensity Lasers" (ICUIL)[111], where they provide an interactive map[112].

PW-class lasers are currently the top class of existing facilities, but several dozens are already too many to list them all. Here we concentrate on facilities and projects significantly exceeding 1 PW.

The Extreme Light Infrastructure (ELI)[113–116] is an advanced laser-based research infrastructure with multi-sites. One of the sites is Extreme Light Infrastructure Nuclear Physics (ELI-NP), which succeeded in delivering the 10 PW @ 1 shot per minute in 2019.

In UK, Central Laser Facility (CLF)[117,118], part of the Rutherford Appleton Laboratory, is dedicated to high-energy laser systems. There are five laser facilities: ULTRA, Artemis, OCTOPUS, Gemini and Vulcan. Here, Gemini is a dual beam laser system with $2\times$ 15 J, 30 fs laser pulses. Vulcan has two kinds of laser modes. In its long pulse mode, the laser energy is up to 2.6 kJ with nanosecond pulse duration. In short pulse mode, it is up to 1 PW peak power with 500 fs pulse duration and the focal intensity is about 10^{21} W/cm^2. Recently, they are going to increase the peak power from 1 PW (500 J in 500 fs) to 20 PW (400 J in 20 fs). It will be a unique beamline to examine matter under extreme conditions.

In France, the Apollon laser system is a multi-beam, multi-petawatt facilities to generate 10 PW pulses of 150 J energy and 15 fs (FWHM) duration at a repetition rate of 1 shot per minute. And the first available laser beam delivered on-target pulses of 10 J average energy, 24 fs duration and 1 PW nominal power in 2021[119].

The Institute of Applied Physics of the Russian Academy of Sciences established a large infrastructure project, the Exawatt Center for Extreme Light Studies (XCELS)[120–122]. The aim of the project is to build high power lasers with 200 PW power, 25 fs pulse duration by assembling 12 identical laser channels with 15 PW power for each. The intensity in the focus is expected to be $\sim 10^{25}$ W/cm^2. That provides an opportunity to peer into the fundamental processes and unknown phenomena of high-energy physics.

Furthermore, the project of Shanghai HIgh repetition rate XFEL aNd Extreme light facility (SHINE) was proceeded[123] in Shanghai, China. In future, the Station of Extreme Light (SEL) of SHINE will provide more brilliant laser system with 100 PW and the expected focused laser intensity is $2 \cdot 10^{23}$ W/cm^2[124]. That is the basis for the proposed experiments[35,77] at SHINE.

In view of vacuum birefringence, the gain of ellipticitiy δ^2 with laser peak intensity is obviously quite strong, $\delta^2 \propto (I_{\rm BG})^2$, see Eq. (16a). This is in particular important for the trade-off of ellipticity against the purity $\mathcal{P}$. Table 4 shows that an intensity of $I_{\rm BG} \sim 2 \cdot 10^{23}$ W/cm^2 can yield an ellipticity $\delta^2 \sim 2 \cdot 10^{-10}$, exceeding the best purities so far measured, $\mathcal{P} \sim 10^{-11}$, cf. Tab. 3. That way, the signal would always exceed the background from the finite extinction. In addition it should be noted that such intensity was already demonstrated with a 4 PW laser system[109].

3.4.3. Combined facilities For the purpose of vacuum birefringence experiments where the background field is generated by an ultra-intense laser and X-ray polarimetry is employed for detection, it is mandatory to combine XFELs with such lasers. In most cases, XFEL facilities host several beamlines and/or several instruments per beamline. Thanks to the wide range of applications and thus an existing market, it is relatively straightforward to equip an XFEL instrument with an ultra-intense laser. Even for systems below the PW level are enough use cases to use XFELs as probe in laser-matter interactions.

Referring to Tab. 5, there are 3 out of 4 existing hard X-ray facilities equipped with an ultra-intense laser. We can exclude soft X-ray FELs since a key for detection is a short probe wavelength. The facilities and instruments are: MEC at LCLS/SLAC, SACLA EH6 and HED/HIBEF at European XFEL. Their respective parameters[35,91,98,111,125–127] are listed in Table 6.

The Matter in Extreme Conditions (MEC) instrument is the facility at LCLS to produce extreme matter states with an intense laser radiation where LCLS provides complete imaging and optical diagnostics methods. Nagler *et al.*[125] presented an overview of the beamline, the capabilities of the instrumentation and highlights of experiments. Glenzer *et al.*[130] summarized the first experiment of laser-compressed solids and with the measurements of highly accurate X-ray diffraction and X-ray Thomson scattering on the MEC instrument at LCLS. Fletcher *et al.*[131] investigated bremsstrahlung from relativistic electrons generated by the interaction of a high-intensity femtosecond laser with solid μm-thick aluminum and polypropylene targets, and measured the energy spectrum and temperature of hot electrons via the differential X-ray energy filtering.

Similar to the LCLS, the SACLA XFEL facility opened after completion of the commissioning[127,132]. This experimental platform is equipped with two beams of 800 nm wavelength, 1 Hz repetition rate, 12.5 J maximum energy of in a 25 fs pulse duration and a 500 TW peak power after pulse compression. Yabuuchi *et al.*[127] characterized the light source performance during the commissioning of the experimental platform and confirmed the XFEL and the high-intensity laser can operate normally with dedicated diagnostics.

In Europe, the High Energy Density (HED) scientific instrument at the European XFEL is a unique platform for experiments at extreme conditions of pressure, temperature,

https://doi.org/10.1017/hpl.2023.45 Published online by Cambridge University Press

Facility	Endstation	E_{BG}	τ_{BG}	P_{BG}	I_{BG}
LCLS	MEC[125]	1 J	40 fs	25 TW	$\leq 10^{20}\,\mathrm{W/cm^2}$
LCLS-II(-HE)	*MEC-U[126]*	150 J	150 fs	1 PW	$>10^{21}\,\mathrm{W/cm^2}$
European XFEL	HED[128,129]	10 J	30 fs	300 TW	$\leq 10^{22}\,\mathrm{W/cm^2}$
SACLA	EH6[127]	2×12.5 J	30 fs	2×500 TW	$\leq 10^{21}\,\mathrm{W/cm^2}$
SHINE	*SEL[35]*	1500J	15 fs	100 PW	$>10^{23}\,\mathrm{W/cm^2}$

Table 6: Overview of facilities combining XFEL beams with PW-class lasers. Planned facilities are printed italic. Please note that there is no common factorial relation between laser power and peak intensity. Focussing F-numbers very among the facilities, adapted to their overall mission. Furthermore, beam quality can reduce the encircled energy in the focal spot and therefore reduce the peak intensity[127]. Provided laser pulse wavefront control for the final focussing and reasonably tight focussing, $10^{22}\,\mathrm{W/cm^2}$ per 1 PW is realistic.

or electromagnetic field[128,133]. Zastrau *et al.*[128] presented the scientific scope, technical infrastructure, diagnostics and experimental platforms. The HED scientific instrument supports a variety of X-ray methods, including X-ray polarimetry. The Helmholtz International Beamline for Extreme Fields (HIBEF) user consortium (UC) contributes the high-intensity and high-energy laser systems[129][134] and their operation for users.

Another combined XFEL – laser facility will be the station of extreme light (SEL) at SHINE, which is designed to achieve laser intensities sufficient to explore the vacuum birefringence effect by colliding a XFEL[35][135].

In view of vacuum birefringence, currently operating facilities provide laser intensities of 10^{19}–$10^{21}\,\mathrm{W/cm^2}$[125,127,129]. Thus ellipticities should be expected to $\sim10^{-14}$, much smaller than the currently best polarization purities. Reasons for those comparably low intensities can be a) operating at lower energy and power levels due to longer lifetime and cost efficiency, b) not too tight focussing for target debris managements (for laser-matter interactions) and c) wavefront distortions, re-distributing energy out of the focus peak into a halo.

Those restrictions can be lifted for experiments dedicated to vacuum birefringence, e.g. providing a dedicated focussing element. We repeat here that a peak intensity of $\sim10^{23}\,\mathrm{W/cm^2}$ was already demonstrated with a 4 PW laser system[109]. That said, the laser at the HED instrument of European XFEL could reach with slightly more energy (12.5 J) and shorter pulse duration (25 fs) a peak power of 400 TW and thus $\sim10^{22}\,\mathrm{W/cm^2}$ peak intensity, resulting in an ellipticity of $6\cdot10^{-12}$ instead of $4\cdot10^{-13}$ as estimated by Mosman *et al.*[85].

3.4.4. X-ray optics Besides precision X-ray polarizers, compound refractive lenses (CRLs) are indispensable optical elements in the vacuum birefringence experimental setup with two purposes. Primarily, the XFEL beam must be focused into the interaction volume with the tightly focused PW laser. That is the purpose of the first CRL. On the other hand, the polarizers require a low divergence to provide a high extinction ratio. Therefore, the first CRLs must be located after the polarizer. In addition, XFEL must be recollimated by the second CRL, after the interaction but before the analyzer. In essence, two sets of CRLs are already inside the polarimeter setup. Therefore, the effects of the CRL material on the polarization must be studied and a suitable material must be found. Grabiger *et al.*[61] studied how the lens material itself influences the X-ray polarization. The setup is shown in Figure 13[61].

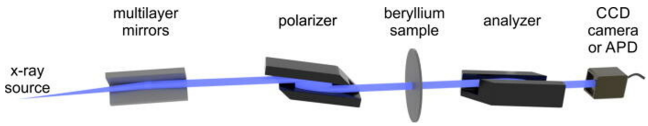

Figure 13: Sketch of the experimental setup investigating CRL material properties. The multilayer mirrors collimate the X-rays from the rotating anode X-ray source. The combination of the polarizer, analyzer, and CCD camera allows for polarization sensitive imaging. Taken from Grabiger *et al.*[61].

They analyzed three different grades of beryllium samples: high purity (PF-60), optical grade (O-30-H), and ultra-high purity grade (IF-1) beryllium. The results in the upper part of Table 7 clearly show that the Beryllium samples greatly affect polarization purity. In this regard, the explanation given by the authors is the polycrystalline state of beryllium and they suggested two better options to focus X-rays. One alternative way is to employ reflective optical components, such as Kirkpatrick–Baez mirrors. Another option is to manufacture X-ray lenses from either single-crystal material like diamond, or from materials with an amorphous structure such as glassy carbon and polymers.

Those materials were studied later by the same group[72]. They used now a synchrotron source for better sensitivity and investigated the impact of CRLs of different materials on the polarization purity, mimicking the general scheme of focussing and recollimation, proposed for vacuum birefringence X-ray polarimetry experiments[19,33,35,84,86]. However, they employed rather long focal lengths of $\sim6\,\mathrm{m}$. For shorter focal lengths, more CRL material would be exposed to the beam and probably deteriorating the purity stronger than

https://doi.org/10.1017/hpl.2023.45 Published online by Cambridge University Press

currently measured. The results are listed in the lower part of Table 7. CRLs were fabricated out of Be, SU-8 photo-polymer, diamond and glassy carbon. From all those materials, the CRLs fabricated from SU-8, did show the least depolarization of X-rays.

Sample	Thickness (μm)	Polarization purity
No sample	-	$8 \cdot 10^{-8}$
Be PF-60	500	$9 \cdot 10^{-6}$
Be IF-1	500	$6 \cdot 10^{-6}$
Be O-30-H	700	$4 \cdot 10^{-6}$
CRL Material	**Transmission**	**Polarization purity**
No lenses	-	$(1.4 \pm 0.9) \cdot 10^{-11}$
Be O-30-H	0.93	$(6.9 \pm 0.2) \cdot 10^{-9}$
SU-8	0.64	$(3.3 \pm 1.5) \cdot 10^{-11}$
Diamond	0.82	$(3.1 \pm 0.7) \cdot 10^{-10}$
Glassy carbon	0.63	$(1.9 \pm 0.1) \cdot 10^{-9}$

Table 7: Deterioration of polarization purity by CRL materials. Upper part for flat Be samples at $\sim$8 keV; lower part for CRLs telescopes with $2 \times \sim$6 m focal length at $\sim$13 keV. Data taken from Grabiger *et al.* and Marx-Glowna *et al.* [61,72].

It should be noted that data for Be cannot be easily compared across both parts of Table 7. The effective thickness of the Be CRLs is not provided, and both experiments employed different photon energies.

In regard of X-ray polarimetry for vacuum birefringence, the results show another limit. Even though the deteriorated purity $(3.3 \pm 1.5) \cdot 10^{-11}$ is close to the instrument purity $(1.4 \pm 0.9) \cdot 10^{-11}$, the deterioration was measurable. Without speculating about scalings, a birefringence experiment using CRLs as currently known would have a limit of at least the measured level of $\mathcal{P} \sim 10^{-11}$. Hence, the prospects for lowering the background signal $NT\mathcal{P}$ by better X-ray optics are dismal.

3.5. Interim summary

An attractive application of X-ray polarimetry is to detect the vacuum birefringence phenomenon. There is one widely recognized method, combining PW optical lasers with XFELs. Alternatively two XFEL pulses, out of a pulse train or by a split-and-delay setup, are proposed. Such scheme appears currently more demanding in terms of X-ray beam path setup.

So far, X-ray polarizer technology has made tremendous progress, cf. Tab. 3. Material dependencies, beam dependencies (divergence, Eq. (7)) and sophisticated alignment protocols (detour avoidance by azimuth alignment) are understood and have become practice. Despite that the transition from synchrotrons to XFELs for polarizer characterization allows for better purity due to the divergence dependence, the spectral width of XFELs is not matching that of polarizers, leading to low throughput. That limits the polarimeter in terms of photon flux: Only very few photons arrive at the detector [59]. This can be optimized by spectral tailoring of the FEL process as well as increasing the acceptance of channel-cut crystals by using asymmetric cuts and appropriate polarizer material choice.

That optimization of integrated transmission is mandatory for X-ray polarimetry of vacuum birefringence in order to provide a high signal photon number $NT\delta^2$ per pulse. Since both the spectral bandwidth of a reflection as well as the temporal pulse stretching depend the effective penetration depth, appropriate material selection (high Z) could optimize both effects simultaneously. This is in contradiction to high peak reflectivity and the avoidance of detour reflections which limit the polarization purity $\mathcal{P}$, where it was found that their contribution in the overall reflected beam grows strongly with Z.

It was further recognized that CRL lens material might affect the polarization purity as CRLs are foreseen in most schemes for vacuum birefringence. The first investigation of traditional CRL lens material [61] was an important step towards applications of polarimetry, and has shown the need for further investigations and improvements of purity. A follow-up study, employing actual CRL telescopes (as often proposed for vacuum birefringence studies) but fabricated from unconventional materials, showed [72] that those materials have much reduced impact on the purity.

As this impact is probably limiting the purity $\mathcal{P}$, the ratio of signal to background, $\delta^2/\mathcal{P}$, must be improved by increasing the ellipticity δ^2. This is possible due to the strong scaling with laser peak intensity, $\delta^2 \propto I_{\mathrm{BG}}^2$, cf. Eq. (16a). Thereby also the absolute signal photon number $NT\delta^2$ increases, reducing the number of required laser pulses.

In summary, measurements of vacuum birefringence in laboratory conditions from ultra-intense lasers by X-ray polarimetry are still pending and need proper preparation in regard of source photon count, beam divergence, spectral transmission, polarizer reflectivity, CRL transmission and depolarization, polarizer extinction, and detector efficiency.

4. Further applications of X-ray polarimetry

Apart from probing vacuum birefringence, X-ray polarimetry is applied to other scientific cases: nuclear resonant scattering experiments [68,136–138], measuring the magnetic fields inside solid density plasmas via Faraday rotation [139–141] and applications to astrophysics [34,82,142,143]. Now, we present those applications of X-ray polarimetry.

4.1. Nuclear resonant scattering

Nuclear resonant scattering is a technique for measuring the structural dynamics, magnetic and electronic properties of condensed matter. Compared to usual radioactive sources, synchrotron radiation sources open new perspectives for

https://doi.org/10.1017/hpl.2023.45 Published online by Cambridge University Press

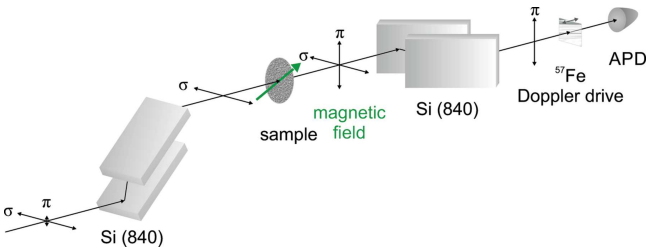

Figure 14: Schematic setup for nuclear resonant scattering with the polarization filtering method. The incoming radiation from the left is polarized by the first channel-cut crystal. Subsequently, the beam impinges on the magnetically anisotropic sample under investigation. The green arrow indicates the direction of the external magnetic field that induces optical activity via X-ray magnetic linear dichroism. The analyzer crystal in the crossed setting transmits only the photons which have undergone nuclear resonant σ- to π–scattering. Taken from Marx-Glowna *et al.*[68].

nuclear resonant scattering in the field of materials science[67,68,144]. Polarimetry with perfect crystals is adequate for preventing the non-resonant scattering called polarization filtering in nuclear resonant scattering experiments[67,68,145]. The elementary idea is to separate non-resonant scattering from a large background of resonantly scattered X-rays. The schematic setup is displayed in Figure 14[68]. The polarizer and analyzer are Silicon (840) channel-cut crystals with two asymmetric reflections and are in the crossed position. Linearly polarized radiation will switch its polarization to mix polarization states when it is scattered by a medium placed in a magnetic field upon nuclear resonant reflection. π–components can pass through but σ–components are strongly suppressed by the analyzer in crossed position. Thereby, the pump photons can be sufficiently suppressed while the relatively weak signal can be detected.

4.2. *Detection of magnetic fields*

In 1990, Siddons *et al.*[16] observed the rotation of the polarization plane of a synchrotron X-ray beam in cobalt alloys by X-ray polarimetry, thereby detecting the optical Faraday effect in the X-ray domain. They also demonstrated the optical activity near the K-edge of cobalt in a chiral organometallic compound.

Faraday rotation is also a widely used diagnostic of plasmas[146,147], usually employing visible lasers in low-density plasmas, e.g. magnetic confinement fusion plasmas[148]. With XFELs, this method can be transferred to solid-density plasmas. This is of great interest for plasmas driven by ultrashort und ultra-intense lasers to probe the self-generated magnetic fields[139]. The fields reach kilo- to megatesla-level (MT) field strength and originate from fast electron transport, balancing return currents and their respective resistivity inside the solid target[141]. Researchers[139–141] have proposed a method of examining the magnetic fields of the laser-irradiated plasma by X-ray polarimetry via Faraday rotation using XFELs.

Figure 15 depicts the experimental setup[140]. The optical ultra-short relativistic laser pulse is deployed to generate extreme multi-megagauss (MG) magnetic fields in a solid-density target. The XFEL acts as a probe to detect those laser-driven magnetic fields. The probe XFEL beam is perfectly horizontally polarized, and then the orientation of the polarization plane is rotated by the magnetic field component. The total rotation angle of the exiting XFEL beam is[139,140]:

$$\phi_{\mathrm{rot}} = \frac{e_0}{2\,c\,m_{\mathrm{e}}} \int \frac{n_{\mathrm{e}}(\mathbf{r})}{n_{\mathrm{c}}}\,\mathbf{B}(\mathbf{r}) \cdot \frac{\mathbf{k}}{|\mathbf{k}|}\,\mathrm{d}s \qquad (19)$$

with e_0 the electron's charge, c the speed of light, m_{e} the electron's rest mass and $\int \mathrm{d}s$ the integral along the probe beam path. n_{e} is the electron density and $\mathbf{k}$ is the wave vector of the probe. The critical density n_{c} is defined by

$$n_{\mathrm{c}} = \frac{\varepsilon_0\, m_{\mathrm{e}}\, \omega^2}{e_0^2} = \frac{\varepsilon_0\, m_{\mathrm{e}}\, 4\pi^2\, c^2}{e_0^2\, \lambda^2}\,, \qquad (20)$$

being the highest electron density in which a wave with wavelength $\lambda = 2\pi/|\mathbf{k}|$ can propagate.

From equations (19) and (20) we can see that the rotation angle is proportional to the wavelength of the probe beam. A beam with a long wavelength can obtain a large rotation angle but will have poor penetration depth in solid density plasma. However, even though the wavelength of XFEL is short, the XFEL is able to penetrate solid density plasmas of up to several tens of micrometer thicknesses because of the high attenuation length. Therefore, it is advantageous to select the XFEL beam as the probe pulse. The studies proposing this scheme[139,141] estimate that the polarization of an XFEL with $6.457\,\mathrm{keV}$ photon energy will be rotated about $\pm 300\,\mu\mathrm{rad}$. The two signs arise from the symmetry to the electron current axis where fields are parallel or anti-parallel to the probe beam direction. An order of $10^{-4}\,\mathrm{rad}$ does not require utmost polarization purity, in contrast to vacuum birefringence. Nevertheless, for an imaging application, overall transmission is important due to beam size magnification.

4.3. *Astrophysics*

X-ray polarimetry is an appealing tool to investigate geometric information, emission mechanisms and the structure of the magnetic fields in and around objects in the universe, such as supermassive black holes and neutron stars[34,82,142,143,149]. In astrophysics, the formation and subsequent evolution of the population of black holes is fascinating and can be determined by the mass and angular momentum given by X-ray polarimetry[142]. In 1976,

https://doi.org/10.1017/hpl.2023.45 Published online by Cambridge University Press

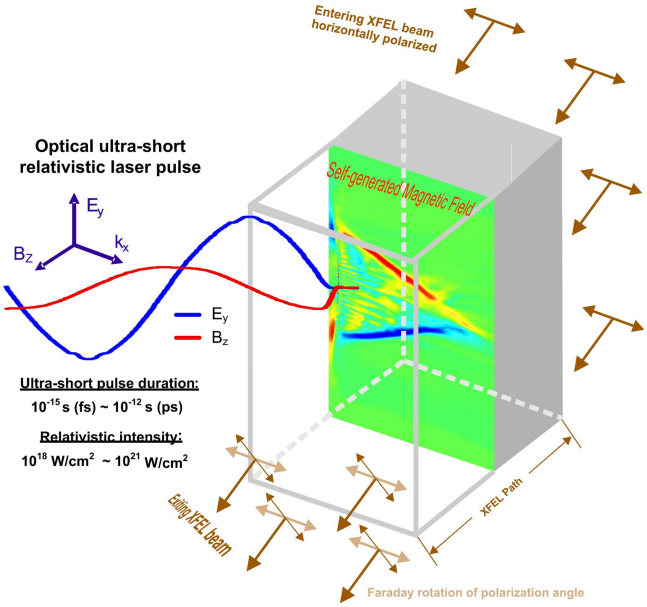

Figure 15: An illustrated experimental setup of strong magnetic field generation by interaction of an ultra-short relativistic optical laser pulse with solid matter, probed by an XFEL via Faraday rotation. Taken from Huang *et al.*[140].

Weisskopf *et al.*[149] measured the linear polarization of the X-ray flux from the Crab Nebula by the graphite crystal X-ray polarimeters aboard the OSO-8 satellite, as illustrated in Figure 16[149]. For reducing the background signal from cosmic rays, the parabolic surface is used to focus the diffracted X-rays. Caiazzo *et al.*[82] presents that vacuum birefringence affects changes of the X-ray polarization of stellar-mass and supermassive black holes. The model with QED not only can probe the spin and the magnetic field strength close to the innermost stable orbit of black-hole accretion disks but also provides a validity check for theories of astrophysical accretion. For accretion-powered pulsars with known energy of cyclotron-resonant scattering features[150], X-ray polarimetry is suited to obtain informations of the geometry of the accretion column and magnetic field strength. Besides, X-ray polarimetry has the potential to discover the mechanisms of astrophysical particle acceleration, like supernova remnants (SNRs), pulsar wind nebulae (PWNe), pulsars, and black hole jets[143]. Heyl and Caiazzo[34] applied the equation of the polarization evolution to determine the atmosphere composition and the surface gravity of an X-ray pulsar. Furthermore, the radius of the star can be inferred from the photon energy at the polarization direction flips. Therefore, X-ray polarimetry is a powerful tool to study neutron stars and black holes. Its high sensitivity and resolution are promising to unravel crucial information of physical processes and structure of astronomical objects.

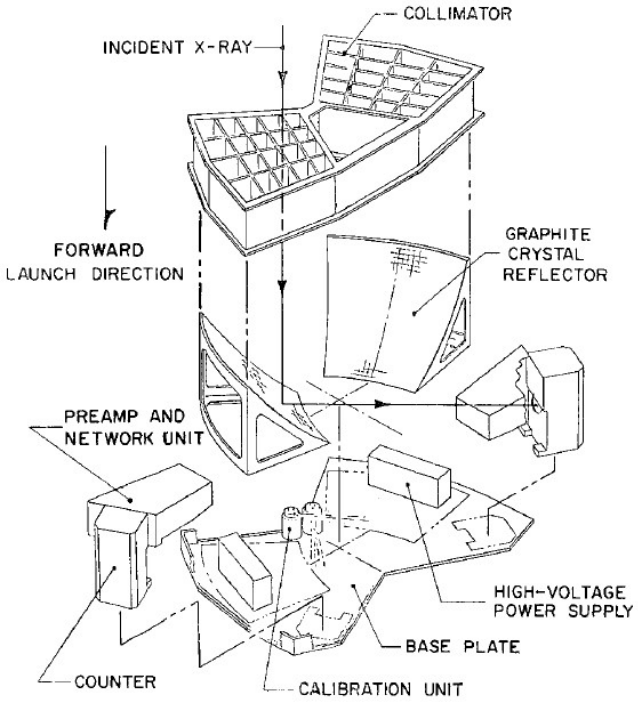

Figure 16: Exploded view of the OSO-8 polarimeter assemblies. The crystal reflector employs $\sim 45°$ Bragg angle and is thereby polarization-filtering. Taken from Novik *et al.*[151].

5. Conclusions

This paper reviews the status of X-ray polarimetry and mainly its application on detecting vacuum birefringence. First, the main details of the factors affecting the polarization purity of X-rays were analyzed for $45°$ Bragg reflectors, employing Brewster's law for suppression of a linear component in the plane of incidence. Crystal quality, beam quality and material dependencies were presented and detailed for channel-cut crystal polarizers. An unprecedented polarization purity of $1.4 \cdot 10^{-11}$ was measured so far[72] at a synchrotron thanks to the average high flux, such that divergence reduction still allowed for precise measurements. A measurement at an XFEL yielded $8 \cdot 10^{-11}$[59]. There, the divergence would have allowed for 10^{-14}, yet the setup was not as optimized as at the synchrotron, and the effectice flux was insufficient for precise characterization. However, the record at the synchrotron is limited by the divergence, and substantial future improvements are subject to XFELs.

This high level of polarization purity provides an opportunity to explore the nonlinear property of vacuum, like vacuum birefringence. An all-optical laboratory scheme allows for precise measurements of QED nonlinearities in particular in the low-energy but strong-field limit, sensitive to new physics and particles beyond the standard model[21,38]. For this application, we summarized for various proposals the signal dependence on ultra-intense laser sources which offer

https://doi.org/10.1017/hpl.2023.45 Published online by Cambridge University Press

extremely intense external fields to polarize the vacuum. We presented the scientific facilities of optical PW lasers and XFELs in the world. We assessed their status regarding proposed experimental schemes and added aspects beyond the sole polarization purity $\mathcal{P}$ and ellipticity δ^2, relevant in the entirety of the proposed schemes. What is more, the X-ray polarimetry has a wide range of applications in nuclear resonant scattering experiments and measuring the magnetic fields inside solid density plasmas, even astrophysics. In brief, the X-ray polarimetry is an extraordinary method and it provides scientists with the possibility to explore the unknown.

Acknowledgement

The author Qiqi Yu (File No. 201908310159) would like to thank the financial support by the China Scholarship Council. Support by the High Energy Density Department at Helmholtz-Zentrum Dresden – Rossendorf is gratefully acknowledged. The authors thank the support by the Ministry of Science and Technology of the People's Republic of China (Grant No. 2018YFA0404803) and the National Natural Science Foundation of China (Grant No. 11935008). We would like to thank Kai Sven Schulze, Robert Loetzsch, Berit Marx-Glowna, Ingo Uschmann, Gerhard G. Paulus, Felix Karbstein, Holger Gies, Lingen Huang, Jörg Grenzer and Roland Sauerbrey for fruitful discussions.

References

1. J Clerk Maxwell. VIII. A dynamical theory of the electromagnetic field. *Philosophical Transactions of the Royal Society of London*, 155:459–512, dec 1865.
2. Frans Snik, Julia Craven-Jones, Michael Escuti, Silvano Fineschi, David Harrington, Antonello De Martino, Dimitri Mawet, Jérôme Riedi, and J. Scott Tyo. An overview of polarimetric sensing techniques and technology with applications to different research fields. In David B. Chenault and Dennis H. Goldstein, editors, *Polarization: Measurement, Analysis, and Remote Sensing XI*, volume 9099, page 90990B. International Society for Optics and Photonics, SPIE, 2014.
3. Markus Axer, Katrin Amunts, David Grässel, Christoph Palm, Jürgen Dammers, Hubertus Axer, Uwe Pietrzyk, and Karl Zilles. A novel approach to the human connectome: Ultra-high resolution mapping of fiber tracts in the brain. *NeuroImage*, 54(2):1091–1101, 2011.
4. Oleg Dubovik, Zhengqiang Li, Michael I. Mishchenko, Didier Tanré, Yana Karol, Bojan Bojkov, Brian Cairns, David J. Diner, W. Reed Espinosa, Philippe Goloub, Xingfa Gu, Otto Hasekamp, Jin Hong, Weizhen Hou, Kirk D. Knobelspiesse, Jochen Landgraf, Li Li, Pavel Litvinov, Yi Liu, Anton Lopatin, Thierry Marbach, Hal Maring, Vanderlei Martins, Yasjka Meijer, Gennadi Milinevsky, Sonoyo Mukai, Frederic Parol, Yanli Qiao, Lorraine Remer, Jeroen Rietjens, Itaru Sano, Piet Stammes, Snorre Stamnes, Xiaobing Sun, Pierre Tabary, Larry D. Travis, Fabien Waquet, Feng Xu, Changxiang Yan, and Dekui Yin. Polarimetric remote sensing of atmospheric aerosols: Instruments, methodologies, results, and perspectives. *Journal of Quantitative Spectroscopy and Radiative Transfer*, 224:474–511, February 2019.
5. Cheng Chen, Oleg Dubovik, Gregory L. Schuster, Mian Chin, Daven K. Henze, Tatyana Lapyonok, Zhengqiang Li, Yevgeny Derimian, and Ying Zhang. Multi-angular polarimetric remote sensing to pinpoint global aerosol absorption and direct radiative forcing. *Nature Communications*, 13(1), December 2022.
6. Tatiana Novikova, Angelo Pierangelo, Antonello De Martino, Abdelali Benali, and Pierre Validire. Polarimetric imaging for cancer diagnosis and staging. *Opt. Photon. News*, 23(10):26–33, Oct 2012.
7. Charles G. Barkla. Polarisation in Röntgen Rays. *Nature*, 69(1794):463, 1904.
8. Charles G. Barkla. Secondary röntgen radiation. *Nature*, 71(1845):440–440, March 1905.
9. Charles G. Barkla. Secondary rontgen rays and atomic weight. *Nature*, 73(1894):365–365, February 1906.
10. P. Skalicky and C. Malgrange. Polarization phenomena in X-ray diffraction. *Acta Crystallographica Section A*, 28(6):501–507, Nov 1972.
11. Michael Hart. X-ray polarization phenomena. *Philosophical Magazine B*, 38(1):41–56, jul 1978.
12. Hiroyuki Ohsumi and Taka hisa Arima. Novel insight into structural magnetism by polarized synchrotron x-ray scattering. *Advances in Physics: X*, 1(1):128–145, 2016.
13. Yoshihiko Togawa, Yusuke Kousaka, Katsuya Inoue, and Jun-ichiro Kishine. Symmetry, structure, and dynamics of monoaxial chiral magnets. *Journal of the Physical Society of Japan*, 85(11):112001, 2016.
14. S. L. Zhang, G. van der Laan, and T. Hesjedal. Direct experimental determination of spiral spin structures via the dichroism extinction effect in resonant elastic soft x-ray scattering. *Phys. Rev. B*, 96:094401, Sep 2017.
15. Annika T. Schmitt, Yves Joly, Kai S. Schulze, Berit Marx-Glowna, Ingo Uschmann, Benjamin Grabiger, Hendrik Bernhardt, Robert Loetzsch, Amélie Juhin, Jérôme Debray, Hans-Christian Wille, Hasan Yavaş, Gerhard G. Paulus, and Ralf Röhlsberger. Disentangling x-ray dichroism and birefringence via high-purity polarimetry. *Optica*, 8(1):56, jan 2021.
16. D P Siddons, M. Hart, Y Amemiya, and J. B. Hastings. X-ray optical activity and the Faraday effect in cobalt and its compounds. *Physical Review Letters*, 64(16):1967–1970, apr 1990.

https://doi.org/10.1017/hpl.2023.45 Published online by Cambridge University Press

17. W. Heisenberg and H. Euler. Folgerungen aus der diracschen theorie des positrons. In *Original Scientific Papers / Wissenschaftliche Originalarbeiten*, pages 162–180. Springer Berlin Heidelberg, 1989.
18. N. Ahmadiniaz, T. E. Cowan, R. Sauerbrey, U. Schramm, H.-P. Schlenvoigt, and R. Schützhold. Heisenberg limit for detecting vacuum birefringence. *Physical Review D*, 101(11), June 2020.
19. Hans-Peter Schlenvoigt, Tom Heinzl, Ulrich Schramm, Thomas E Cowan, and Roland Sauerbrey. Detecting vacuum birefringence with x-ray free electron lasers and high-power optical lasers: a feasibility study. *Physica Scripta*, 91(2):023010, January 2016.
20. Thomas Heinzl, Ben Liesfeld, Kay-Uwe Amthor, Heinrich Schwoerer, Roland Sauerbrey, and Andreas Wipf. On the observation of vacuum birefringence. *Optics Communications*, 267(2):318–321, November 2006.
21. H. Gies. Strong laser fields as a probe for fundamental physics. *The European Physical Journal D*, 55(2):311–317, 2009.
22. W H Furry. A Symmetry Theorem in the Positron Theory. *Physical Review*, 51(2):125–129, jan 1937.
23. Willis E Lamb and Robert C Retherford. Fine Structure of the Hydrogen Atom by a Microwave Method. *Phys.˜Rev.*, 72:241–243, 1947.
24. D Hanneke, S Fogwell, and G Gabrielse. New Measurement of the Electron Magnetic Moment and the Fine Structure Constant. *Phys.˜Rev.˜Lett.*, 100:120801, 2008.
25. E D Commins. Electron Spin and Its History. *Ann.˜Rev.˜Nucl.˜Part.˜Sci.*, 62:133–157, 2012.
26. James P. Miller, Rafael Eduardo de, B. Lee Roberts, and Dominik Stöckinger. Muon (g 2): Experiment and Theory. *Annual Review of Nuclear and Particle Science*, 62(1):237–264, 2012.
27. Paul Papatzacos and Kjell Mork. Delbrück scattering. *Physics Reports*, 21(2):81–118, September 1975.
28. A.I. Milstein and Martin Schumacher. Present status of Delbrück scattering. *Physics Reports*, 243(4):183–214, jul 1994.
29. E Brezin and C Itzykson. Polarization Phenomena in Vacuum Nonlinear Electrodynamics. *Physical Review D*, 3(2):618–621, jan 1971.
30. M. Marklund and J. Lundin. Quantum vacuum experiments using high intensity lasers. *The European Physical Journal D*, 55(2):319–326, June 2009.
31. Victor Dinu, Tom Heinzl, Anton Ilderton, Mattias Marklund, and Greger Torgrimsson. Vacuum refractive indices and helicity flip in strong-field QED. *Physical Review D*, 89(12), June 2014.
32. B. King and T. Heinzl. Measuring vacuum polarization with high-power lasers. *High Power Laser Science and Engineering*, 4, 2016.
33. Felix Karbstein and Chantal Sundqvist. Probing vacuum birefringence using x-ray free electron and optical high-intensity lasers. *Physical Review D*, 94(1), July 2016.
34. Jeremy Heyl and Ilaria Caiazzo. Strongly magnetized sources: QED and x-ray polarization. *Galaxies*, 6(3):76, July 2018.
35. Baifei Shen, Zhigang Bu, Jiancai Xu, Tongjun Xu, Liangliang Ji, Ruxin Li, and Zhizhan Xu. Exploring vacuum birefringence based on a 100 PW laser and an x-ray free electron laser beam. *Plasma Physics and Controlled Fusion*, 60(4):044002, February 2018.
36. Felix Karbstein. Probing vacuum polarization effects with high-intensity lasers. *Particles*, 3(1):39–61, January 2020.
37. B. King and N. Elkina. Vacuum birefringence in high-energy laser-electron collisions. *Physical Review A*, 94(6), December 2016.
38. W T Hill and L Roso. Probing the quantum vacuum with petawatt lasers. *Journal of Physics: Conference Series*, 869:012015, July 2017.
39. A. Fedotov, A. Ilderton, F. Karbstein, B. King, D. Seipt, H. Taya, and G. Torgrimsson. Advances in QED with intense background fields. *Physics Reports*, 1010:1–138, April 2023.
40. Stefan Ataman. Vacuum birefringence detection in all-optical scenarios. *Physical Review A*, 97(6), June 2018.
41. A. Ejlli, F. Della Valle, U. Gastaldi, G. Messineo, R. Pengo, G. Ruoso, and G. Zavattini. The PVLAS experiment: A 25 year effort to measure vacuum magnetic birefringence. *Physics Reports*, 871:1–74, August 2020.
42. J. Agil, R. Battesti, and C. Rizzo. Vacuum birefringence experiments: optical noise. *The European Physical Journal D*, 76(10), October 2022.
43. Sheng-Jui Chen, Hsien-Hao Mei, and Wei-Tou Ni. Q&A experiment to search for vacuum dichroism, pseudoscalar–photon interaction and millicharged fermions. *Modern Physics Letters A*, 22(37):2815–2831, December 2007.
44. Hsien-Hao Mei, Wei-Tou Ni, Sheng-Jui Chen, and Sheau-Shi Pan. Axion search with Q & A experiment. *Modern Physics Letters A*, 25(11n12):983–993, 2010.
45. H. Cole, F. W. Chambers, and C. G. Wood. X-ray polarizer. *Journal of Applied Physics*, 32(10):1942–1945, October 1961.
46. Gerhard Borrmannn. Über Extinktionsdiagramme der Röntgenstrahlen von Quarz. *Physikalische Zeitschrift*, 42:157–162, 1941.
47. Boris W. Batterman and Henderson Cole. Dynamical diffraction of x rays by perfect crystals. *Reviews of Modern Physics*, 36(3):681–717, July 1964.
48. K. S. Schulze, B. Marx, I. Uschmann, E. Förster, T. Stöhlker, and G. G. Paulus. Determination of

https://doi.org/10.1017/hpl.2023.45 Published online by Cambridge University Press

the polarization state of x rays with the help of anomalous transmission. *Applied Physics Letters*, 104(15):151110, April 2014.

49. Dennis M. Mills. Techniques of production and analysis of polarized synchrotron radiation. In James P. Knauer and Gopal K. Shenoy, editors, *SPIE Proceedings*. SPIE, January 1991.
50. Fabio Muleri, Paolo Soffitta, Ronaldo Bellazzini, Alessandro Brez, Enrico Costa, Massimo Frutti, Marcello Mastropietro, Ennio Morelli, Michele Pinchera, Alda Rubini, and Gloria Spandre. A versatile facility for the calibration of x-ray polarimeters with polarized and unpolarized controlled beams. In Martin J. L. Turner and Kathryn A. Flanagan, editors, *Space Telescopes and Instrumentation 2008: Ultraviolet to Gamma Ray*. SPIE, July 2008.
51. B. Marx, K. S. Schulze, I. Uschmann, T. Kämpfer, R. Lötzsch, O. Wehrhan, W. Wagner, C. Detlefs, T. Roth, J. Härtwig, E. Förster, T. Stöhlker, and G. G. Paulus. High-precision x-ray polarimetry. *Physical Review Letters*, 110(25), June 2013.
52. K. S. Schulze. Fundamental limitations of the polarization purity of x rays. *APL Photonics*, 3(12):126106, December 2018.
53. Hendrik Bernhardt, Berit Marx-Glowna, Kai S. Schulze, Benjamin Grabiger, Johann Haber, Carsten Detlefs, Robert Loetzsch, Tino Kämpfer, Ralf Röhlsberger, Eckhart Förster, Thomas Stöhlker, Ingo Uschmann, and Gerhard G. Paulus. High purity x-ray polarimetry with single-crystal diamonds. *Applied Physics Letters*, 109(12):121106, September 2016.
54. M. Hart and A. R. D. Rodrigues. Tuneable polarizers for x-rays and neutrons. *Philosophical Magazine B*, 40(2):149–157, August 1979.
55. Hendrik Bernhardt, Annika T. Schmitt, Benjamin Grabiger, Berit Marx-Glowna, Robert Loetzsch, Hans-Christian Wille, Dimitrios Bessas, Aleksandr I. Chumakov, Rudolf Rüffer, Ralf Röhlsberger, Thomas Stöhlker, Ingo Uschmann, Gerhard G. Paulus, and Kai S. Schulze. Ultra-high precision x-ray polarimetry with artificial diamond channel cuts at the beam divergence limit. *Physical Review Research*, 2(2), June 2020.
56. Thomas Tschentscher, Christian Bressler, Jan Grünert, Anders Madsen, Adrian Mancuso, Michael Meyer, Andreas Scherz, Harald Sinn, and Ulf Zastrau. Photon beam transport and scientific instruments at the european XFEL. *Applied Sciences*, 7(6):592, June 2017.
57. M. Renninger. Umweganregung, eine bisher unbeachtete wechselwirkungserscheinung bei raumgitterinterferenzen. *Zeitschrift für Physik*, 106(3-4):141–176, March 1937.
58. B. Marx, I. Uschmann, S. Höfer, R. Lötzsch, O. Wehrhan, E. Förster, M. Kaluza, T. Stöhlker, H. Gies, C. Detlefs, T. Roth, J. Härtwig, and G.G. Paulus. Determination of high-purity polarization state of x-rays. *Optics Communications*, 284(4):915–918, February 2011.
59. Kai S. Schulze, Benjamin Grabiger, Robert Loetzsch, Berit Marx-Glowna, Annika T. Schmitt, Alejandro Laso Garcia, Willi Hippler, Lingen Huang, Felix Karbstein, Zuzana Konôpková, Hans-Peter Schlenvoigt, Jan-Patrick Schwinkendorf, Cornelius Strohm, Toma Toncian, Ingo Uschmann, Hans-Christian Wille, Ulf Zastrau, Ralf Röhlsberger, Thomas Stöhlker, Thomas E. Cowan, and Gerhard G. Paulus. Towards perfectly linearly polarized x-rays. *Physical Review Research*, 4(1), March 2022.
60. Berit Marx-Glowna, Kai S. Schulze, Ingo Uschmann, Tino Kämpfer, Günter Weber, Christoph Hahn, Hans-Christian Wille, Kai Schlage, Ralf Röhlsberger, Eckhart Förster, Thomas Stöhlker, and Gerhard G. Paulus. Influence of higher harmonics of the undulator in x-ray polarimetry and crystal monochromator design. *Journal of Synchrotron Radiation*, 22(5):1151–1154, July 2015.
61. Benjamin Grabiger, Berit Marx-Glowna, Ingo Uschmann, Robert Loetzsch, Gerhard G. Paulus, and Kai S. Schulze. A highly sensitive imaging polarimeter in the x-ray regime. *Applied Physics Letters*, 117(20):201102, November 2020.
62. Jens Als-Nielsen and Des McMorrow. *Elements of Modern X-ray Physics*. John Wiley & Sons Ltd, 2011.
63. J. Z. Tischler and B. W. Batterman. Determination of phase using multiple-beam effects. *Acta Crystallographica Section A Foundations of Crystallography*, 42(6):510–514, November 1986.
64. U. Bonse and M. Hart. Tailless X-ray single-crystal reflection curves obtained by multiple reflection. *Applied Physics Letters*, 7(9):238–240, November 1965.
65. Jesse W. M. DuMond. Theory of the use of more than two successive x-ray crystal reflections to obtain increased resolving power. *Physical Review*, 52(8):872–883, October 1937.
66. E.E. Alp, W. Sturhahn, and T.S. Toellner. Polarizer–analyzer optics. *Hyperfine Interactions*, 125(1/4):45–68, 2000.
67. T. S. Toellner, E. E. Alp, W. Sturhahn, T. M. Mooney, X. Zhang, M. Ando, Y. Yoda, and S. Kikuta. Polarizer/analyzer filter for nuclear resonant scattering of synchrotron radiation. *Applied Physics Letters*, 67(14):1993–1995, October 1995.
68. Berit Marx-Glowna, Ingo Uschmann, Kai S. Schulze, Heike Marschner, Hans-Christian Wille, Kai Schlage, Thomas Stöhlker, Ralf Röhlsberger, and Gerhard G. Paulus. Advanced x-ray polarimeter design for nuclear

https://doi.org/10.1017/hpl.2023.45 Published online by Cambridge University Press

resonant scattering. *Journal of Synchrotron Radiation*, 28(1):120–124, January 2021.

69. Yuri Shvyd'ko, Stanislav Stoupin, Vladimir Blank, and Sergey Terentyev. Near-100% bragg reflectivity of x-rays. *Nature Photonics*, 5(9):539–542, August 2011.
70. Yuri Shvyd'Ko and Ryan Lindberg. Spatiotemporal response of crystals in x-ray Bragg diffraction. *Physical Review Special Topics - Accelerators and Beams*, 15(10):1–24, 2012.
71. Jaromír Hrdý. X-ray pulse stretching after diffraction. *Journal of Applied Crystallography*, 53:623–628, 2020.
72. B Marx-Glowna, B Grabiger, R Lötzsch, I Uschmann, A T Schmitt, K S Schulze, A Last, T Roth, S Antipov, H-P Schlenvoigt, I Sergueev, O Leupold, R Röhlsberger, and G G Paulus. Scanning high-sensitive x-ray polarization microscopy. *New Journal of Physics*, 24(5):053051, May 2022.
73. A. Di Piazza, C. Müller, K. Z. Hatsagortsyan, and C. H. Keitel. Extremely high-intensity laser interactions with fundamental quantum systems. *Reviews of Modern Physics*, 84(3):1177–1228, August 2012.
74. O. Borysov, B. Heinemann, A. Ilderton, B. King, and A. Potylitsyn. Using the nonlinear breit-wheeler process to test nonlinear vacuum birefringence. *Physical Review D*, 106(11), December 2022.
75. Bai Song Xie, Zi Liang Li, and Suo Tang. Electron-positron pair production in ultrastrong laser fields. *Matter and Radiation at Extremes*, 2(5):225–242, September 2017.
76. In Ko, Heung-Sik Kang, Hoon Heo, Changbum Kim, Gyujin Kim, Chang-Ki Min, Haeryong Yang, Soung Baek, Hyo-Jin Choi, Geonyeong Mun, Byoung Park, Young Suh, Dong Shin, Jinyul Hu, Juho Hong, Seonghoon Jung, Sang-Hee Kim, KwangHoon Kim, Donghyun Na, Soung Park, Yong Park, Young Jung, Seong Jeong, Hong Lee, Sangbong Lee, Sojeong Lee, Bonggi Oh, Hyung Suh, Jang-Hui Han, Min Kim, Nam-Suk Jung, Young-Chan Kim, Mong-Soo Lee, Bong-Ho Lee, Chi-Won Sung, Ik-Su Mok, Jung-Moo Yang, Yong Parc, Woul-Woo Lee, Chae-Soon Lee, Hocheol Shin, Ji Kim, Yongsam Kim, Jae Lee, Sang-Youn Park, Jangwoo Kim, Jaeku Park, Intae Eom, Seungyu Rah, Sunam Kim, Ki Hyun Nam, Jaehyun Park, Jaehun Park, Sangsoo Kim, Soonnam Kwon, Ran An, Sang Park, Kyung Kim, Hyojung Hyun, Seung Kim, Seonghan Kim, Chung-Jong Yu, Bong-Soo Kim, Tai-Hee Kang, Kwang-Woo Kim, Seung-Hwan Kim, Hee-Seock Lee, Heung-Soo Lee, Ki-Hyeon Park, Tae-Yeong Koo, Dong-Eon Kim, and Ki Lee. Construction and commissioning of PAL-XFEL facility. *Applied Sciences*, 7(5):479, May 2017.
77. Dirui Xu, Baifei Shen, Jiancai Xu, and Zhenfeng Liang. XFEL beamline design for vacuum birefringence experiment. *Nuclear Instruments and Methods in Physics Research Section A: Accelerators, Spectrometers, Detectors and Associated Equipment*, 982:164553, December 2020.
78. James K. Koga, Masakatsu Murakami, Alexey V. Arefiev, and Yoshihide Nakamiya. Probing and possible application of the QED vacuum with micro-bubble implosions induced by ultra-intense laser pulses. *Matter and Radiation at Extremes*, 4(3):034401, May 2019.
79. R. Taverna, F. Muleri, R. Turolla, P. Soffitta, S. Fabiani, and L. Nobili. Probing magnetar magnetosphere through x-ray polarization measurements. *Monthly Notices of the Royal Astronomical Society*, 438(2):1686–1697, December 2013.
80. R. P. Mignani, V. Testa, D. González Caniulef, R. Taverna, R. Turolla, S. Zane, and K. Wu. Evidence for vacuum birefringence from the first optical-polarimetry measurement of the isolated neutron star RX j1856.5-3754. *Monthly Notices of the Royal Astronomical Society*, 465(1):492–500, November 2016.
81. L. M. Capparelli, A. Damiano, L. Maiani, and A. D. Polosa. A note on polarized light from magnetars. *The European Physical Journal C*, 77(11), November 2017.
82. Ilaria Caiazzo and Jeremy Heyl. Vacuum birefringence and the x-ray polarization from black-hole accretion disks. *Physical Review D*, 97(8), April 2018.
83. Yuto Minami and Eiichiro Komatsu. New extraction of the cosmic birefringence from the planck 2018 polarization data. *Physical Review Letters*, 125(22), November 2020.
84. Felix Karbstein, Holger Gies, Maria Reuter, and Matt Zepf. Vacuum birefringence in strong inhomogeneous electromagnetic fields. *Physical Review D*, 92(7):071301, oct 2015.
85. Elena A. Mosman and Felix Karbstein. Vacuum birefringence and diffraction at an x-ray free-electron laser: From analytical estimates to optimal parameters. *Physical Review D*, 104(1):13006, 2021.
86. Felix Karbstein, Chantal Sundqvist, Kai S Schulze, Ingo Uschmann, Holger Gies, and Gerhard G Paulus. Vacuum birefringence at x-ray free-electron lasers. *New Journal of Physics*, 23(9):095001, September 2021.
87. Taito Osaka, Ichiro Inoue, Jumpei Yamada, Yuichi Inubushi, Shotaro Matsumura, Yasuhisa Sano, Kensuke Tono, Kazuto Yamauchi, Kenji Tamasaku, and Makina Yabashi. Hard x-ray intensity autocorrelation using direct two-photon absorption. *Phys. Rev. Res.*, 4:L012035, Mar 2022.
88. A. Schropp, P. Boye, J. M. Feldkamp, R. Hoppe, J. Patommel, D. Samberg, S. Stephan, K. Gieweke-

https://doi.org/10.1017/hpl.2023.45 Published online by Cambridge University Press

meyer, R. N. Wilke, T. Salditt, J. Gulden, A. P. Mancuso, I. A. Vartanyants, E. Weckert, S. Schöder, M. Burghammer, and C. G. Schroer. Hard x-ray nanobeam characterization by coherent diffraction microscopy. *Applied Physics Letters*, 96(9):2–4, 2010.

89. Andreas Schropp, Robert Hoppe, Vivienne Meier, Jens Patommel, Frank Seiboth, Hae Ja Lee, Bob Nagler, Eric C. Galtier, Brice Arnold, Ulf Zastrau, Jerome B. Hastings, Daniel Nilsson, Fredrik Uhlén, Ulrich Vogt, Hans M. Hertz, and Christian G. Schroer. Full spatial characterization of a nanofocused X-ray free-electron laser beam by ptychographic imaging. *Scientific Reports*, 3:1–5, 2013.
90. Yoshihide Nakamiya and Kensuke Homma. Probing vacuum birefringence under a high-intensity laser field with gamma-ray polarimetry at the GeV scale. *Physical Review D*, 96(5), September 2017.
91. Nanshun Huang, Haixiao Deng, Bo Liu, Dong Wang, and Zhentang Zhao. Features and futures of X-ray free-electron lasers. *The Innovation*, 2(2):100097, 2021.
92. W. Ackermann, G. Asova, V. Ayvazyan, A. Azima, N. Baboi, J. Bähr, V. Balandin, B. Beutner, A. Brandt, A. Bolzmann, R. Brinkmann, O. I. Brovko, M. Castellano, P. Castro, L. Catani, E. Chiadroni, S. Choroba, A. Cianchi, J. T. Costello, D. Cubaynes, J. Dardis, W. Decking, H. Delsim-Hashemi, A. Delserieys, G. Di Pirro, M. Dohlus, S. Düsterer, A. Eckhardt, H. T. Edwards, B. Faatz, J. Feldhaus, K. Flöttmann, J. Frisch, L. Fröhlich, T. Garvey, U. Gensch, Ch. Gerth, M. Görler, N. Golubeva, H.-J. Grabosch, M. Grecki, O. Grimm, K. Hacker, U. Hahn, J. H. Han, K. Honkavaara, T. Hott, M. Hüning, Y. Ivanisenko, E. Jaeschke, W. Jalmuzna, T. Jezynski, R. Kammering, V. Katalev, K. Kavanagh, E. T. Kennedy, S. Khodyachykh, K. Klose, V. Kocharyan, M. Körfer, M. Kollewe, W. Koprek, S. Korepanov, D. Kostin, M. Krassilnikov, G. Kube, M. Kuhlmann, C. L. S. Lewis, L. Lilje, T. Limberg, D. Lipka, F. Löhl, H. Luna, M. Luong, M. Martins, M. Meyer, P. Michelato, V. Miltchev, W. D. Möller, L. Monaco, W. F. O. Müller, O. Napieralski, O. Napoly, P. Nicolosi, D. Nölle, T. Nuñez, A. Oppelt, C. Pagani, R. Paparella, N. Pchalek, J. Pedregosa-Gutierrez, B. Petersen, B. Petrosyan, G. Petrosyan, L. Petrosyan, J. Pflüger, E. Plönjes, L. Poletto, K. Pozniak, E. Prat, D. Proch, P. Pucyk, P. Radcliffe, H. Redlin, K. Rehlich, M. Richter, M. Roehrs, J. Roensch, R. Romaniuk, M. Ross, J. Rossbach, V. Rybnikov, M. Sachwitz, E. L. Saldin, W. Sandner, H. Schlarb, B. Schmidt, M. Schmitz, P. Schmüser, J. R. Schneider, E. A. Schneidmiller, S. Schnepp, S. Schreiber, M. Seidel, D. Sertore, A. V. Shabunov, C. Simon, S. Simrock, E. Sombrowski, A. A. Sorokin, P. Spanknebel, R. Spesyvtsev, L. Staykov, B. Steffen, F. Stephan, F. Stulle, H. Thom, K. Tiedtke, M. Tischer, S. Toleikis, R. Treusch, D. Trines, I. Tsakov, E. Vogel, T. Weiland, H. Weise, M. Wellhöfer, M. Wendt, I. Will, A. Winter, K. Wittenburg, W. Wurth, P. Yeates, M. V. Yurkov, I. Zagorodnov, and K. Zapfe. Operation of a free-electron laser from the extreme ultraviolet to the water window. *Nature Photonics*, 1(6):336–342, June 2007.
93. Deutsches Elektronen-Synchrotron DESY Ein Forschungszentrum der Helmholtz-Gemeinschaft. https://www.desy.de/. Accessed: 2023-01-26.
94. Italian Elettra Sincrotrone Trieste. https://www.elettra.eu/. Accessed: 2023-01-26.
95. Christopher Milne, Thomas Schietinger, Masamitsu Aiba, Arturo Alarcon, Jürgen Alex, Alexander Anghel, Vladimir Arsov, Carl Beard, Paul Beaud, Simona Bettoni, Markus Bopp, Helge Brands, Manuel Brönnimann, Ingo Brunnenkant, Marco Calvi, Alessandro Citterio, Paolo Craievich, Marta Csatari Divall, Mark Dällenbach, Michael D'Amico, Andreas Dax, Yunpei Deng, Alexander Dietrich, Roberto Dinapoli, Edwin Divall, Sladana Dordevic, Simon Ebner, Christian Erny, Hansrudolf Fitze, Uwe Flechsig, Rolf Follath, Franziska Frei, Florian Gärtner, Romain Ganter, Terence Garvey, Zheqiao Geng, Ishkhan Gorgisyan, Christopher Gough, Andreas Hauff, Christoph Hauri, Nicole Hiller, Tadej Humar, Stephan Hunziker, Gerhard Ingold, Rasmus Ischebeck, Markus Janousch, Pavle Juranić, Mario Jurcevic, Maik Kaiser, Babak Kalantari, Roger Kalt, Boris Keil, Christoph Kittel, Gregor Knopp, Waldemar Koprek, Henrik Lemke, Thomas Lippuner, Daniel Llorente Sancho, Florian Löhl, Carlos Lopez-Cuenca, Fabian Märki, Fabio Marcellini, Goran Marinkovic, Isabelle Martiel, Ralf Menzel, Aldo Mozzanica, Karol Nass, Gian Orlandi, Cigdem Ozkan Loch, Ezequiel Panepucci, Martin Paraliev, Bruce Patterson, Bill Pedrini, Marco Pedrozzi, Patrick Pollet, Claude Pradervand, Eduard Prat, Peter Radi, Jean-Yves Raguin, Sophie Redford, Jens Rehanek, Julien Réhault, Sven Reiche, Matthias Ringele, Jochen Rittmann, Leonid Rivkin, Albert Romann, Marie Ruat, Christian Ruder, Leonardo Sala, Lionel Schebacher, Thomas Schilcher, Volker Schlott, Thomas Schmidt, Bernd Schmitt, Xintian Shi, Markus Stadler, Lukas Stingelin, Werner Sturzenegger, Jakub Szlachetko, Dhanya Thattil, Daniel Treyer, Alexandre Trisorio, Wolfgang Tron, Seraphin Vetter, Carlo Vicario, Didier Voulot, Meitian Wang, Thierry Zamofing, Christof Zellweger, Riccardo Zennaro, Elke Zimoch, Rafael Abela, Luc Patthey, and Hans-Heinrich Braun. SwissFEL: The swiss x-ray free electron laser. *Applied Sciences*, 7(7):720, July 2017.
96. Paul Scherrer Institut. https://www.psi.ch/en/swissfel. Accessed: 2023-01-26.
97. P Emma, R Akre, J Arthur, R Bionta, C Bostedt,

https://doi.org/10.1017/hpl.2023.45 Published online by Cambridge University Press

J Bozek, A Brachmann, P Bucksbaum, R Coffee, F J Decker, Y Ding, D Dowell, S Edstrom, A Fisher, J Frisch, S Gilevich, J Hastings, G Hays, HeringPh, Z Huang, R Iverson, H Loos, M Messerschmidt, A Miahnahri, S Moeller, H D Nuhn, G Pile, D Ratner, J Rzepiela, D Schultz, T Smith, P Stefan, H Tompkins, J Turner, J Welch, W White, J Wu, G Yocky, and J Galayda. First lasing and operation of an \rangstrom-wavelength free-electron laser. *Nature Photonics*, 4(9):641–647, 2010.

98. Linac Coherent Light Source. https://lcls.slac.stanford.edu/. Accessed: 2023-01-26.
99. J.N. Galayda. The LCLS-II: A High Power Upgrade to the LCLS. In *Proc. 9th International Particle Accelerator Conference (IPAC'18), Vancouver, BC, Canada, April 29-May 4, 2018*, number 9 in International Particle Accelerator Conference, pages 18–23, Geneva, Switzerland, June 2018. JACoW Publishing. https://doi.org/10.18429/JACoW-IPAC2018-MOYGB2.
100. T.O. Raubenheimer. The LCLS-II-HE, A High Energy Upgrade of the LCLS-II. In *Proc. 60th ICFA Advanced Beam Dynamics Workshop (FLS'18), Shanghai, China, 5-9 March 2018*, number 60 in ICFA Advanced Beam Dynamics Workshop, pages 6–11, Geneva, Switzerland, June 2018. JACoW Publishing. https://doi.org/10.18429/JACoW-FLS2018-MOP1WA02.
101. David Pile. First light from SACLA. *Nature Photonics*, 5(8):456–457, July 2011.
102. Makina Yabashi, Hitoshi Tanaka, and Tetsuya Ishikawa. Overview of the SACLA facility. *Journal of Synchrotron Radiation*, 22(3):477–484, May 2015.
103. Kensuke Tono, Toru Hara, Makina Yabashi, and Hitoshi Tanaka. Multiple-beamline operation of SACLA. *Journal of Synchrotron Radiation*, 26(2):595–602, Mar 2019.
104. Bo Liu, Chao Feng, Duan Gu, Fei Gao, Haixiao Deng, Meng Zhang, Sen Sun, Si Chen, Wei Zhang, Wencheng Fang, Zhen Wang, Qiaogen Zhou, Yongbin Leng, Ming Gu, Lixin Yin, Qiang Gu, Guoping Fang, Dong Wang, and Zhentang Zhao. The SXFEL upgrade: From test facility to user facility. *Applied Sciences*, 12(1):176, December 2021.
105. Bai-Fei Shen, Liang-Liang Ji, Xiao-Mei Zhang, Zhi-Gang Bu, Jian-Cai Xu, and and. High field x-ray laser physics. *Acta Physica Sinica*, 70(8):084101, 2021.
106. E.L. Saldin, E.A. Schneidmiller, Yu.V. Shvyd'ko, and M.V. Yurkov. X-ray FEL with a meV bandwidth. *Nuclear Instruments and Methods in Physics Research Section A: Accelerators, Spectrometers, Detectors and Associated Equipment*, 475(1-3):357–362, dec 2001.
107. Gianluca Geloni, Vitali Kocharyan, and Evgeni Saldin. A novel self-seeding scheme for hard X-ray FELs. *Journal of Modern Optics*, 58(16):1391–1403, sep 2011.
108. J. Amann, W. Berg, V. Blank, F.-J. Decker, Y. Ding, P. Emma, Y. Feng, J. Frisch, D. Fritz, J. Hastings, Z. Huang, J. Krzywinski, R. Lindberg, H. Loos, A. Lutman, H.-D. Nuhn, D. Ratner, J. Rzepiela, D. Shu, Yu. Shvyd'ko, S. Spampinati, S. Stoupin, S. Terentyev, E. Trakhtenberg, D. Walz, J. Welch, J. Wu, A. Zholents, and D. Zhu. Demonstration of self-seeding in a hard-X-ray free-electron laser. *Nature Photonics*, 6(10):693–698, oct 2012.
109. Jin Woo Yoon, Yeong Gyu Kim, Il Woo Choi, Jae Hee Sung, Hwang Woon Lee, Seong Ku Lee, and Chang Hee Nam. Realization of laser intensity over 10sup23/sup w/cmsup2/sup. *Optica*, 8(5):630, May 2021.
110. Donna Strickland and Gerard Mourou. Compression of amplified chirped optical pulses. *Optics Communications*, 56(3):219–221, 1985.
111. The International Committee on Ultrahigh Intensity Lasers. https://www.icuil.org/. Accessed: 2023-01-26.
112. Map of all ultra-high intensity laser systems in the world that are known to ICUIL. https://www.easymapmaker.com/map/ICUIL_World_Map_v3. Accessed: 2023-01-26.
113. S Gales, K A Tanaka, D L Balabanski, F Negoita, D Stutman, O Tesileanu, C A Ur, D Ursescu, I Andrei, S Ataman, M O Cernaianu, L D'Alessi, I Dancus, B Diaconescu, N Djourelov, D Filipescu, P Ghenuche, D G Ghita, C Matei, K Seto, M Zeng, and N V Zamfir. The extreme light infrastructure—nuclear physics (ELI-NP) facility: new horizons in physics with 10 PW ultra-intense lasers and 20 MeV brilliant gamma beams. *Reports on Progress in Physics*, 81(9):094301, August 2018.
114. V. Zamfir, K. Tanaka, and C. Ur. Extreme light infrastructure nuclear physics (ELI-NP). *Europhysics News*, 50(2):23–25, March 2019.
115. K. A. Tanaka, K. M. Spohr, D. L. Balabanski, S. Balascuta, L. Capponi, M. O. Cernaianu, M. Cuciuc, A. Cucoanes, I. Dancus, A. Dhal, B. Diaconescu, D. Doria, P. Ghenuche, D. G. Ghita, S. Kisyov, V. Nastasa, J. F. Ong, F. Rotaru, D. Sangwan, P.-A. Söderström, D. Stutman, G. Suliman, O. Tesileanu, L. Tudor, N. Tsoneva, C. A. Ur, D. Ursescu, and N. V. Zamfir. Current status and highlights of the ELI-NP research program. *Matter and Radiation at Extremes*, 5(2):024402, March 2020.
116. Extreme Light Infrastructure. https://eli-laser.eu/. Accessed: 2023-01-26.
117. O. Chekhlov, E. J. Divall, K. Ertel, S. J. Hawkes, C. J. Hooker, I. N. Ross, P. Matousek, C. Hernandez-Gomez, I. Musgrave, Y. Tang, T. Winstone, D. Neely, R. Clarke, P. Foster, S. J. Hancock, B. E. Wyborn,

https://doi.org/10.1017/hpl.2023.45 Published online by Cambridge University Press

and J. L. Collier. Development of petawatt laser amplification systems at the central laser facility. In Vladislav Panchenko, Vladimir Golubev, Andrey Ionin, and Alexander Chumakov, editors, *International Conference on Lasers, Applications, and Technologies 2007: High-Power Lasers and Applications*. SPIE, June 2007.

118. Central Laser Facility. https://www.clf.stfc.ac.uk/Pages/home.aspx. Accessed: 2023-01-26.
119. K. Burdonov, A. Fazzini, V. Lelasseux, J. Albrecht, P. Antici, Y. Ayoul, A. Beluze, D. Cavanna, T. Ceccotti, M. Chabanis, A. Chaleil, S. N. Chen, Z. Chen, F. Consoli, M. Cuciuc, X. Davoine, J. P. Delaneau, E. d'Humières, J.-L. Dubois, C. Evrard, E. Filippov, A. Freneaux, P. Forestier-Colleoni, L. Gremillet, V. Horny, L. Lancia, L. Lecherbourg, N. Lebas, A. Leblanc, W. Ma, L. Martin, F. Negoita, J.-L. Paillard, D. Papadopoulos, F. Perez, S. Pikuz, G. Qi, F. Quéré, L. Ranc, P.-A. Söderström, M. Scisciò, S. Sun, S. Vallières, P. Wang, W. Yao, F. Mathieu, P. Audebert, and J. Fuchs. Characterization and performance of the apollon short-focal-area facility following its commissioning at 1 PW level. *Matter and Radiation at Extremes*, 6(6):064402, November 2021.
120. I.B. Mukhin, A.A. Soloviev, E.A. Perevezentsev, A.A. Shaykin, V.N. Ginzburg, I.V. Kuzmin, M.A. Mart'yanov, I.A. Shaikin, A.A. Kuzmin, S.Yu. Mironov, I.V. Yakovlev, and E.A. Khazanov. Design of the front-end system for a subexawatt laser of the XCELS facility. *Quantum Electronics*, 51(9):759–767, September 2021.
121. Colin N. Danson, Constantin Haefner, Jake Bromage, Thomas Butcher, Jean-Christophe F. Chanteloup, Enam A. Chowdhury, Almantas Galvanauskas, Leonida A. Gizzi, Joachim Hein, David I. Hillier, Nicholas W. Hopps, Yoshiaki Kato, Efim A. Khazanov, Ryosuke Kodama, Georg Korn, Ruxin Li, Yutong Li, Jens Limpert, Jingui Ma, Chang Hee Nam, David Neely, Dimitrios Papadopoulos, Rory R. Penman, Liejia Qian, Jorge J. Rocca, Andrey A. Shaykin, Craig W. Siders, Christopher Spindloe, Sándor Szatmári, Raoul M. G. M. Trines, Jianqiang Zhu, Ping Zhu, and Jonathan D. Zuegel. Petawatt and exawatt class lasers worldwide. *High Power Laser Science and Engineering*, 7, 2019.
122. Exawatt Center for Extreme Light Studies. https://xcels.iapras.ru/. Accessed: 2023-01-26.
123. Zebiao Gan, Lianghong Yu, Cheng Wang, Yanqi Liu, Yi Xu, Wenqi Li, Shuai Li, Linpeng Yu, Xinliang Wang, Xinyan Liu, Junchi Chen, Yujie Peng, Lu Xu, Bo Yao, Xiaobo Zhang, Lingru Chen, Yunhai Tang, Xiaobin Wang, Dinjun Yin, Xiaoyan Liang, Yuxin Leng, Ruxin Li, and Zhizhan Xu. The shanghai superintense ultrafast laser facility (SULF) project. In *Topics in Applied Physics*, pages 199–217. Springer International Publishing, 2021.
124. Xinliang Wang, Xingyan Liu, Xiaoming Lu, Junchi Chen, Yingbin Long, Wenkai Li, Haidong Chen, Xun Chen, Peile Bai, Yanyan Li, Yujie Peng, Yanqi Liu, Fenxiang Wu, Cheng Wang, Zhaoyang Li, Yi Xu, Xiaoyan Liang, Yuxin Leng, and Ruxin Li. 13.4 fs, 0.1 Hz OPCPA front end for the 100 PW-class laser facility. *Ultrafast Science*, 2022, January 2022.
125. Bob Nagler, Brice Arnold, Gary Bouchard, Richard F. Boyce, Richard M. Boyce, Alice Callen, Marc Campell, Ruben Curiel, Eric Galtier, Justin Garofoli, Eduardo Granados, Jerry Hastings, Greg Hays, Philip Heimann, Richard W. Lee, Despina Milathianaki, Lori Plummer, Andreas Schropp, Alex Wallace, Marc Welch, William White, Zhou Xing, Jing Yin, James Young, Ulf Zastrau, and Hae Ja Lee. The matter in extreme conditions instrument at the linac coherent light source. *Journal of Synchrotron Radiation*, 22(3):520–525, April 2015.
126. Gilliss Dyer and Alan Fry. Matter in extreme conditions upgrade (conceptual design report). Technical report, SLAC, October 2021.
127. Toshinori Yabuuchi, Akira Kon, Yuichi Inubushi, Tadashi Togahi, Keiichi Sueda, Toshiro Itoga, Kyo Nakajima, Hideaki Habara, Ryosuke Kodama, Hiromitsu Tomizawa, and Makina Yabashi. An experimental platform using high-power, high-intensity optical lasers with the hard x-ray free-electron laser at SACLA. *Journal of Synchrotron Radiation*, 26(2):585–594, February 2019.
128. Ulf Zastrau, Karen Appel, Carsten Baehtz, Oliver Baehr, Lewis Batchelor, Andreas Berghäuser, Mohammadreza Banjafar, Erik Brambrink, Valerio Cerantola, Thomas E. Cowan, Horst Damker, Steffen Dietrich, Samuele Di Dio Cafiso, Jörn Dreyer, Hans-Olaf Engel, Thomas Feldmann, Stefan Findeisen, Manon Foese, Daniel Fulla-Marsa, Sebastian Göde, Mohammed Hassan, Jens Hauser, Thomas Herrmannsdörfer, Hauke Höppner, Johannes Kaa, Peter Kaever, Klaus Knöfel, Zuzana Konôpková, Alejandro Laso García, Hanns-Peter Liermann, Jona Mainberger, Mikako Makita, Eike-Christian Martens, Emma E. McBride, Dominik Möller, Motoaki Nakatsutsumi, Alexander Pelka, Christian Plueckthun, Clemens Prescher, Thomas R. Preston, Michael Röper, Andreas Schmidt, Wolfgang Seidel, Jan-Patrick Schwinkendorf, Markus O. Schoelmerich, Ulrich Schramm, Andreas Schropp, Cornelius Strohm, Konstantin Sukharnikov, Peter Talkovski, Ian Thorpe, Monika Toncian, Toma Toncian, Lennart Wollenweber, Shingo Yamamoto, and Thomas Tschentscher. The High Energy Density Scientific Instrument at the European XFEL. *Journal of Synchrotron Radiation*, 28(5):1393–1416, August

https://doi.org/10.1017/hpl.2023.45 Published online by Cambridge University Press

2021.

129. A. Laso Garcia, H. Höppner, A. Pelka, C. Bähtz, E. Brambrink, S. Di Dio Cafiso, J. Dreyer, S. Göde, M. Hassan, T. Kluge, J. Liu, M. Makita, D. Möller, M. Nakatsutsumi, T. R. Preston, G. Priebe, H.-P. Schlenvoigt, J.-P. Schwinkendorf, M. Šmíd, A.-M. Talposi, M. Toncian, U. Zastrau, U. Schramm, T. E. Cowan, and T. Toncian. ReLaX: the Helmholtz International Beamline for Extreme Fields high-intensity short-pulse laser driver for relativistic laser–matter interaction and strong-field science using the high energy density instrument at the European X-ray free electron laser facility. *High Power Laser Science and Engineering*, 9:e59, oct 2021.
130. S H Glenzer, L B Fletcher, E Galtier, B Nagler, R Alonso-Mori, B Barbrel, S B Brown, D A Chapman, Z Chen, C B Curry, F Fiuza, E Gamboa, M Gauthier, D O Gericke, A Gleason, S Goede, E Granados, P Heimann, J Kim, D Kraus, M J MacDonald, A J Mackinnon, R Mishra, A Ravasio, C Roedel, P Sperling, W Schumaker, Y Y Tsui, J Vorberger, U Zastrau, A Fry, W E White, J B Hasting, and H J Lee. Matter under extreme conditions experiments at the linac coherent light source. *Journal of Physics B: Atomic, Molecular and Optical Physics*, 49(9):092001, April 2016.
131. L.B. Fletcher, C.B. Curry, M. Gauthier, G.D. Glenn, Z. Chen, E. Cunningham, A. Descamps, M. Frost, E.C. Galtier, P. Heimann, J.B. Kim, M. Mo, B.K. Ofori-Okai, J. Peebles, F. Seiboth, F. Treffert, G.M. Dyer, E.E. McBride, and S.H. Glenzer. Investigation of hard x-ray emissions from terawatt laser-irradiated foils at the matter in extreme conditions instrument of the linac coherent light source. *Journal of Instrumentation*, 17(04):T04004, April 2022.
132. K Tono, T Togashi, Y Inubushi, T Sato, T Katayama, K Ogawa, H Ohashi, H Kimura, S Takahashi, K Takeshita, H Tomizawa, S Goto, T Ishikawa, and M Yabashi. Beamline, experimental stations and photon beam diagnostics for the hard x-ray free electron laser of SACLA. *New Journal of Physics*, 15(8):083035, August 2013.
133. M Nakatsutsumi, K Appel, C Baehtz, B Chen, T E Cowan, S Göde, Z Konopkova, A Pelka, G Priebe, A Schmidt, K Sukharnikov, I Thorpe, Th Tschentscher, and U Zastrau. Femtosecond laser-generated high-energy-density states studied by x-ray FELs. *Plasma Physics and Controlled Fusion*, 59(1):014028, November 2016.
134. N. Ahmadiniaz, M. Bussmann, T.E. Cowan, A. Debus, T. Kluge, and R. Schützhold. Observability of coulomb-assisted quantum vacuum birefringence. *Physical Review D*, 104(1), July 2021.
135. B. King, H. Hu, and B. Shen. Three-pulse photon-photon scattering. *Physical Review A*, 98(2), August 2018.
136. A. Q. R. Baron, Y. Tanaka, S. Goto, K. Takeshita, T. Matsushita, and T. Ishikawa. An x-ray scattering beamline for studying dynamics. *Journal of Physics and Chemistry of Solids*, 61(3):461–465, March 2000.
137. Rudolf Rüffer. Nuclear resonance scattering. *Comptes Rendus Physique*, 9(5-6):595–607, June 2008.
138. T. S. Toellner, A. Alatas, and A. H. Said. Six-reflection meV-monochromator for synchrotron radiation. *Journal of Synchrotron Radiation*, 18(4):605–611, May 2011.
139. L. G. Huang, H.-P. Schlenvoigt, H. Takabe, and T. E. Cowan. Ionization and reflux dependence of magnetic instability generation and probing inside laser-irradiated solid thin foils. *Physics of Plasmas*, 24(10):103115, October 2017.
140. L. G. Huang, H. Takabe, and T. E. Cowan. Maximizing magnetic field generation in high power laser–solid interactions. *High Power Laser Science and Engineering*, 7, 2019.
141. T. Wang, T. Toncian, M. S. Wei, and A. V. Arefiev. Structured targets for detection of megatesla-level magnetic fields through faraday rotation of XFEL beams. *Physics of Plasmas*, 26(1):013105, January 2019.
142. Jeremy D. Schnittman and Julian H. Krolik. X-Ray Polarization From Accreting Black Holes: The Thermal State. *The Astrophysical Journal*, 701(2):1175–1187, July 2009.
143. Henric Krawczynski, Giorgio Matt, Adam R. Ingram, Roberto Taverna, Roberto Turolla, Fabian Kislat, C. C. Teddy Cheung, Andrei Bykov, Kuver Sinha, Haocheng Zhang, Jeremy Heyl, Niccolo Bucciantini, Greg Madejski, Tim Kallman, Keith M. Jahoda, Quin Abarr, Matthew G. Baring, Luca Baldini, Mitchell Begelman, Markus Boettcher, Edward Cackett, Ilaria Caiazzo, Paolo Coppi, Enrico Costa, Jason Dexter, Jean-Francois Fortin, Charles Gammie, Jessica A. Gaskin, Dimitrios Giannios, Pranab Ghosh, Alice K. Harding, Dieter H. Hartmann, Kiyoshi Hayashida, Svetlana G. Jorstad, Philip Kaaret, Takao Kitaguchi, Luca Latronico, Thomas Maccarone, Alan Marscher, Herman Marshall, Mark McConnell, Jon M. Miller, Stephen L. O'Dell, Feryal Oezel, Takashi Okajima, Mark Pearce, Jeremy Perkins, Brian D. Ramsey, Roger W. Romani, Jeremy D. Schnittman, Carmelo Sgro, Paolo Soffitta, Hiromitsu Takahashi, Toru Tamagawa, John Tomsick, Martin C. Weisskopf, and George Younes. Astro2020 science white paper: Using x-ray polarimetry to probe the physics of black holes and neutron stars, 2019.
144. E. Gerdau, R. Rüffer, H. Winkler, W. Tolksdorf, C. P. Klages, and J. P. Hannon. Nuclear bragg diffraction of

https://doi.org/10.1017/hpl.2023.45 Published online by Cambridge University Press

synchrotron radiation in yttrium iron garnet. *Physical Review Letters*, 54(8):835–838, February 1985.

145. R. Röhlsberger, E. Gerdau, R. Rüffer, W. Sturhahn, T.S. Toellner, A.I. Chumakov, and E.E. Alp. X-ray optics for μeV-resolved spectroscopy. *Nuclear Instruments and Methods in Physics Research Section A: Accelerators, Spectrometers, Detectors and Associated Equipment*, 394(1-2):251–255, July 1997.
146. I. H. Hutchinson. *Principles of Plasma Diagnostics*. Cambridge University Press, Cambridge, jul 2002.
147. Sergio E Segre. A review of plasma polarimetry - theory and methods. *Plasma Physics and Controlled Fusion*, 41(2):R57–R100, feb 1999.
148. T. Pisarczyk, A. A. Rupasov, G. S. Sarkisov, and A. S. Shikanov. Faraday-rotation method for magnetic-field diagnostics in a laser plasma. *Journal of Soviet Laser Research*, 11(1):1–32, 1990.
149. M. C. Weisskopf, G. G. Cohen, H. L. Kestenbaum, K. S. Long, R. Novick, and R. S. Wolff. Measurement of the x-ray polarization of the crab nebula. *The Astrophysical Journal*, 208:L125, September 1976.
150. Martin C. Weisskopf, Ronald F. Elsner, Victoria M. Kaspi, Stephen L. O'Dell, George G. Pavlov, and Brain D. Ramsey. X-ray polarimetry and its potential use for understanding neutron stars. In *Neutron Stars and Pulsars*, pages 589–619. Springer Berlin Heidelberg, 2009.
151. R. Novick. Stellar and solar x-ray polarimetry. *Space Science Reviews*, 18(3):389–408, December 1975.

https://doi.org/10.1017/hpl.2023.45 Published online by Cambridge University Press